J. Fluid Mech. (2009), *vol.* 634, *pp.* 359–404. © 2009 Cambridge University Press
doi:10.1017/S0022112009007289 Printed in the United Kingdom

An experimental investigation of a highly accelerated turbulent boundary layer

C. BOURASSA AND F. O. THOMAS†
Center for Flow Physics and Control, Hessert Laboratory, University of Notre Dame,
Notre Dame, IN 46556, USA

(Received 2 April 2007 and in revised form 25 March 2009)

A canonical flat-plate turbulent boundary layer with $Re_\theta = 4590$ is exposed to a favourable mean streamwise pressure gradient sufficient to cause relaminarization. The favourable pressure gradient is generated by a linear contraction, yielding a peak value of the acceleration parameter of $K = 4.4 \times 10^{-6}$ which is sustained for approximately 13 local boundary layer thicknesses. The relaminarization process is characterized by an extensive series of mean flow and turbulence measurements obtained at several representative streamwise locations. In anticipation of the loss of standard log-law behaviour, the local wall shear stress is directly measured using the oil-film interferometry technique. Mean flow measurements show a systematic variation in the Kármán and additive constants with applied streamwise strain rate. The series of measurements also indicate an apparent decoupling of the outer and near-wall regions of the accelerating boundary layer. In accord with this, conditional measurements show that fourth-quadrant sweep events are virtually eliminated, while much less frequent but larger-amplitude near-wall second-quadrant ejection events remain. The reduction in fourth-quadrant sweep events is matched by an observed increase in near-wall third-quadrant events. The consequent reduction in near-wall Reynolds stress correlation and associated cross-stream momentum transport results in a large reduction in c_f for the relaminarized flow.

1. Introduction

In this paper the response of a turbulent boundary layer on a flat plate to the imposition of a strong favourable streamwise pressure gradient is investigated experimentally. This work is focused on examining the change in structure of the boundary layer caused by external flow acceleration sufficient to cause reverse transition. Such a flow is of both fundamental and practical interest. As an example, in-flight measurements on a Boeing 737 transport aircraft by van Dam *et al.* (1993) showed that relaminarization likely occurs on multi-element wings used for high lift. It has been speculated that so-called inverse Reynolds number effects, in which high-lift system performance actually degrades with increased Reynolds number, may be intimately associated with the relaminarization process. This becomes a key issue in the required extrapolation of wind-tunnel data to flight Reynolds number. From a more fundamental standpoint, examination of the response of the turbulent boundary layer to large imposed streamwise strain rates can provide new insights regarding the physical mechanisms at work in non-equilibrium wall-bounded turbulent shear flows.

---

† Email address for correspondence: flint.o.thomas.1@nd.edu

This paper is certainly not the first to consider turbulent boundary layer development in strong favourable pressure gradient (FPG) leading to relaminarization. Section 2 of this paper provides a brief overview of the rather extensive body of literature that exists on relaminarization. This background material serves to motivate the objectives of the current investigation which are described in § 3 and also provides a framework by which aspects unique to this study may be appreciated.

2. Overview of previous studies of highly accelerated turbulent boundary layers

Turbulent boundary layer relaminarization, or 'reverse transition', was first documented by Wilson (1954) while studying heat transfer coefficients on gas turbine blades. In the more than five decades since Wilson's findings, there have been several important experimental investigations focusing on turbulent boundary layer relaminarization. Examples include Launder (1964), Moretti & Kays (1965), Patel & Head (1968), Blackwelder & Kovasznay (1972), Narasimha & Sreenivasan (1973) and more recently Warnack & Fernholz (1998*a*,*b*), Escudier *et al.* (1998), Ichimiya, Nakamura & Yamashita (1998), Escudier, Ramadan & Johnson (2001) and Mukund *et al.* (2006). Scaling relations and a computational model for the wall layer are presented by Finnicum & Hanratty (1988). An excellent review paper was published by Sreenivasan (1982). From these studies, the following generic physical characteristics of the relaminarization process have emerged: (1) a thinning of the boundary layer, (2) a departure of the mean velocity profiles from both the standard 'law of the wall' and the 'law of the wake', (3) an initial decrease followed by a rapid increase in the shape factor, (4) an initial increase in the heat transfer and skin friction coefficients followed by a substantial decrease, (5) a decrease in the relative turbulence intensity, (6) a rapid decline of turbulent bursting events in the wall layer, (7) a spreading of turbulent intermittency from the outer layer to the wall layer and (8) a decay of the turbulent Reynolds stresses in the near-wall region. Launder (1964) documented an energy shift towards low wavenumbers in both the near-wall region and the outer-region of the boundary layer. Launder commented that the shift towards lower wavenumber implies that an increasing fraction of the turbulence assumes a passive role in the boundary layer development. It also has been observed that the spectra of highly accelerated turbulent boundary layers deviate from the $k^{-5/3}$ roll-off associated with the inertial sub-range of fully developed turbulence. For a turbulent boundary layer undergoing relaminarization, Warnack & Fernholz (1998*b*) showed an increase in the streamwise integral length scale Λ_x/δ by as much as a factor of four and a decrease in the wall-normal integral length scale Λ_y/δ by a factor of two when compared with corresponding values for a zero pressure gradient (ZPG) turbulent boundary layer. Thus a streamwise elongation of the large-eddy structure due to the large FPG was implied. When emerging from an FPG region into a ZPG environment, the structures show definite history effects attributed to flow acceleration. More recently, Mukund *et al.* (2006) demonstrated that for an accelerated turbulent boundary layer that develops on a surface with convex streamwise curvature, the relaminarization process occurs more rapidly than on a flat surface.

Relaminarization appears to occur gradually, and as such, the onset of relaminarization has been difficult to precisely define. Parameters that have been used to define the onset of relaminarization are summarized in table 1 along with their corresponding characteristic values. The most common parameter associated

Author	Parameter	Definition	Value
Launder (1964)	K	$\frac{\nu}{U^2}\frac{\mathrm{d}U}{\mathrm{d}x}$	$\simeq 3.0\times 10^{-6}$
Launder (1964)	H	$\frac{\delta^*}{\theta}$	$\min(H)$
Patel (1965)	Δp	$\frac{\nu}{\rho u_\tau^3}\frac{\mathrm{d}P}{\mathrm{d}x}$	$\simeq -0.025$
Patel & Head (1968)	$\Delta\tau$	$\frac{\nu}{\rho u_\tau^3}\frac{\mathrm{d}\tau}{\mathrm{d}y}$	$\simeq -0.009$
Blackwelder & Kovasznay (1972)	K	$\frac{\nu}{U^2}\frac{\mathrm{d}U}{\mathrm{d}x}$	$\simeq 3.6\times 10^{-6}$

TABLE 1. Non-dimensional parameters and their reported values at the onset of relaminarization.

with relaminarization is a form of the Reynolds number,

$$K=\frac{\nu}{U(x)^2}\frac{\mathrm{d}U(x)}{\mathrm{d}x}, \tag{2.1}$$

where $U(x)$ is the streamwise velocity. First proposed by Launder (1963), relaminarization has been observed to correspond to a value of $K\geqslant 3\times 10^{-6}$, although values in the range of $2.8\times 10^{-6}\leqslant K\leqslant 3.4\times 10^{-6}$ have been reported. For this investigation, K will be referred to as 'the acceleration parameter'. Patel (1965) proposed a non-dimensional pressure gradient parameter

$$\Delta p=\frac{\nu}{\rho u_\tau^3}\frac{\mathrm{d}p(x)}{\mathrm{d}x}, \tag{2.2}$$

since the observed departure from the universal log-law behaviour is reasonably attributed to the pressure gradient. Patel & Head (1968) also proposed a non-dimensional shear stress gradient parameter $\Delta\tau$ in which the pressure gradient in (2.2) is replaced with the shear stress gradient $\mathrm{d}\tau/\mathrm{d}y$. Narasimha & Sreenivasan (1973) observed Δp to reach a minimum upstream of where Patel & Head (1968) inferred the onset of relaminarization; they also claimed similar behaviour for $\Delta\tau$. Narasimha & Sreenivasan (1979) observed that the non-dimensional parameters reach their cited relaminarization values upstream of where the turbulent boundary layer actually reverts to a laminar-like state; in this manner the non-dimensional parameters predict deviation from standard boundary layer behaviour, but they do not necessarily guarantee relaminarization will take place.

In addition to the non-dimensional parameters discussed above, investigations have associated the onset of relaminarization with other observations of the highly accelerated turbulent boundary layer. For example, Badri Narayanan & Ramjee (1969) observed the onset of relaminarization to correspond with a decrease in the turbulence intensity. Kline, Reynolds, Schraub & Runstadler (1967) observed the cessation of turbulent bursting in the near-wall region for the relaminarized boundary layer. In fact, based on flow visualization, Kline *et al.* (1967) educed a value of $K=3.5\times 10^{-6}$ to correspond with a cessation of bursting and that the burst parameter declines exponentially towards zero when scaled as

$$F^+=\frac{F\nu^2}{u_\tau^3}, \tag{2.3}$$

where F is the rate of burst occurrences per unit span. Narasimha & Sreenivasan (1979) found the bursting rate decreases exponentially in a highly accelerated turbulent boundary layer, but the boundary layer never completely ceases bursting, or no obvious extrapolation of F^+ to zero is observed.

With regard to a relaminarization mechanism, Launder (1964) commented that as a boundary layer is exposed to a large FPG the turbulent structure in the near-wall region begins to depart from its ZPG equilibrium state. It was conjectured that this gives rise to a situation in which dissipation exceeds turbulence production, resulting in relaminarization of the turbulent boundary layer. However, measurements by Badri Narayanan, Rajagopalan & Narasimha (1977) above $y/\delta \geqslant 0.1$ indicate that dissipation never exceeds production in an accelerated turbulent boundary layer, although both were observed to be reduced.

Sreenivasan (1982) proposed a two-layer model to explain the relaminarization mechanism. Comprised of the emergence of a viscous inner layer, characterized by the rapid decay of the initial turbulence, and an inviscid outer layer in which the Reynolds stress is 'frozen', Sreenivasan (1982) argued that relaminarization is the result of the 'domination of pressure forces over the slowly responding Reynolds stresses in the outer-layer, accompanied by the generation of a new laminar sub-boundary layer, which itself is maintained stable by the acceleration.' In this model, the turbulent structure is distorted (rather than destroyed) in the outer layer by the rapid flow acceleration. The newly developed viscous inner layer is the result of decaying upstream turbulence. The two layers interact weakly, insofar as they only provide the appropriate boundary conditions. Narasimha & Sreenivasan (1979) found application of eigenfunction theory in the inner layer and rapid distortion theory in the outer layer predicted streamwise turbulence intensity levels, although the wall-normal component was not well predicted.

3. Objectives and organization

The objective of this investigation is to document the streamwise development of an initially canonical flat-plate turbulent boundary layer that is exposed to a favourable streamwise pressure gradient characterized by an acceleration parameter in excess of that typically associated with relaminarization (3.0×10^{-6}). While there have been many investigations of the accelerated boundary layer as described in § 2, unique aspects of this study include the following:

(i) Direct measurement of the local wall shear stress, using the oil-film interferometry (OFI) technique.

(ii) A turbulent boundary layer with $Re_\theta \approx 4600$ upstream of the FPG. This value is larger than in previous experimental studies of relaminarization.

(iii) A maximum acceleration parameter of $K = 4.5 \times 10^{-6}$ with a sustained streamwise exposure to this maximum K value for a distance of 15 cm, or $x/\delta_\circ = 1$ (which corresponds to a local value of $x/\delta \approx 13$).

(iv) A large wind-tunnel facility allows the growth of a comparatively thick boundary layer which, in combination with the utilization of miniature X-wire probes, increases the effective spatial resolution of multi-component velocity fluctuation measurements in the near-wall region.

Results presented in this investigation include the global boundary layer parameters and their dependence on applied pressure gradient, the streamwise evolution of the mean velocity profiles, behaviour of the time-averaged turbulence quantities in the accelerated boundary layer and, finally, the effects of acceleration on the

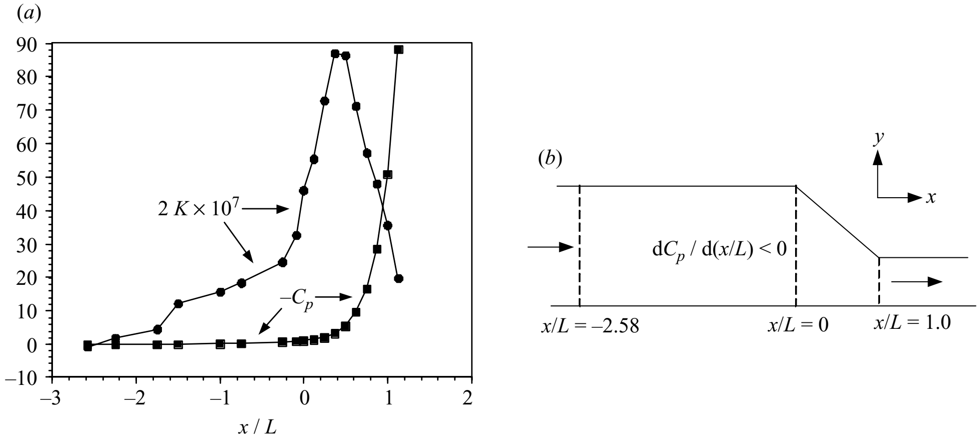

FIGURE 1. (*a*) Static pressure distribution and acceleration parameter K. (*b*) Wind-tunnel geometry and nomenclature.

near-wall boundary layer dynamics being investigated by means of conditional measurements. The paper concludes with a discussion of the experimental results within the framework of wall turbulence generation mechanisms and a description of the conceptual model of the relaminarization process.

4. Experimental apparatus

The measurements of the accelerated turbulent boundary layer were conducted in an in-draft wind-tunnel facility located at the University of Notre Dame. The tunnel has a cross-sectional area of 1.5 m × 1.5 m, a working test-section length of 15.25 m and a maximum free-stream operating speed of approximately 13.5 m s^{-1}. The tunnel inlet has a contraction ratio of 4 : 1. Operating at a free-stream velocity of $U_e = 4.5$ m s^{-1}, the free-stream turbulence intensity measured downstream of the inlet was less than 0.4 %. The wind tunnel is constructed of 0.75 in. plywood and has a Plexiglas sidewall for optical access. To allow the application of silicone oil for use in the OFI technique, a glass sub-floor of width 0.1524 m was embedded flush with the tunnel floor along the centreline of the wind tunnel from 8.99 m to 10.00 m as measured from the entrance of the wind tunnel. Static pressure taps were installed in the floor of the tunnel beside the glass sub-floor every 0.0254 m, beginning at 8.99 m through to 9.75 m.

The design of the wind-tunnel test section was motivated by the need to expose a turbulent boundary layer to a region of large FPG corresponding to a value of the acceleration parameter $K \geqslant 3.0 \times 10^{-6}$. For this investigation, an internal linear contraction with a length of 0.61 m in the flow direction and an angle of 60° (with respect to the top wall of the wind tunnel) was positioned 9.14 m from the entrance of the wind tunnel. In this manner there was a region of substantial turbulent boundary layer growth prior to application of flow acceleration. This internal geometry corresponds to a contraction ratio of 9.5:1 The resulting streamwise variation in mean velocity $U(x)$ and acceleration parameter $K(x)$ will be fully documented in the following section.

For convenience, the linear contraction inlet will be referred to as the '$x = 0$' location, and all streamwise distances x will be normalized by the contraction length $L = 0.61$ m (see figure 1 for a schematic diagram). Throughout the remainder of

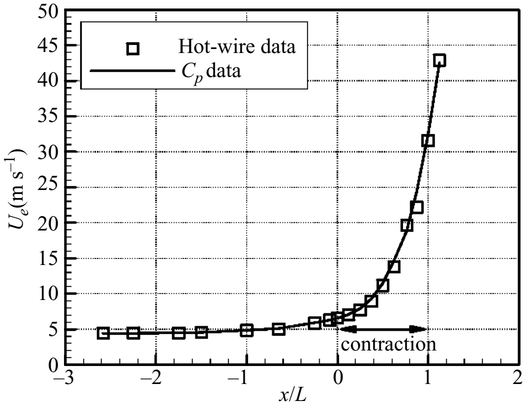

FIGURE 2. External streamwise velocity distribution in the wind tunnel, measured using hot-wire anemometry and derived from the C_p data shown in figure 1.

this paper streamwise distance is defined as positive downstream of the contraction entrance and negative upstream. Therefore the contraction entrance and exit are located at $x/L = 0$ and $x/L = 1.0$, respectively.

5. Streamwise pressure distribution

To determine the wall pressure distribution, static pressure ports mounted in the floor of the wind tunnel were connected to a Scanivalve rotary multiplexer, and the output was directed to a 5 in. H_2O differential electronic manometer. The voltage output of the manometer was measured using a PC data acquisition system with a sampling frequency of 1 kHz and a record length of 30 000 samples. Upstream of the contraction where wall static pressure ports were not available, the streamwise pressure distribution was determined with the use of the static tap of a Pitot-static probe traversed just above the wall along the centreline of the wind tunnel.

The measured streamwise static pressure distribution is presented in figure 1. Also shown is the corresponding experimentally determined acceleration parameter K. For this investigation, the reference pressure was chosen to be the tunnel free-stream pressure upstream of the commencement of flow acceleration at $x/L = -2.58$. The measured maximum value of the acceleration parameter is $K = 4.4 \times 10^{-6}$. The maximum K value is sustained for approximately 15 cm, or $\Delta x/L = 0.25$, within the contraction. The nominal ZPG environment was found to extend from the wind-tunnel inlet to $x/L = -2.58$. Thus the start of mild flow acceleration is located at $x/L = -2.58$ (well upstream of the contraction inlet), and all ZPG reference values will correspond to the boundary layer at this location. The external streamwise velocity distribution throughout the acceleration region is presented in figure 2 as measured using constant-temperature hot-wire anemometry and as derived from the pressure distribution shown in figure 1; good agreement can be seen between the two independent measurement techniques.

6. Initial ZPG turbulent boundary layer characteristics

6.1. *Hot-wire calibration*

In order to measure the three fluctuating velocity components, two types of Auspex miniature X-wires (models AHWX-101 and AHWX-102) were employed. One X-wire was in a 90° configuration and was used to simultaneously measure the streamwise and wall-normal components of velocity. A second straight shaft X-wire was used to simultaneously measure the streamwise and spanwise components of velocity. Both X-wires used tungsten wires of 5 μm diameter and a wire length of approximately 1.25 mm. The 90° X-wire allowed for measurements to be taken to within 0.45 mm of the wall, while the straight shaft X-wire allowed for measurements to within 2.0 mm of the wall. An AA Lab Systems 10-channel constant temperature anemometer system was used in conjunction with the X-wire probes. Frequency response of the X-wires was determined to be in the range of 28–32 kHz using a square-wave test. All hot-wire data were digitally recorded using a 10 kHz sampling frequency and a record length of 400 000 samples. A 5 kHz low-pass analogue filter was used for all measurements to prevent temporal aliasing. The raw voltages from the anemometer were recorded to both optical media and a hard drive for post-processing and archival storage.

The X-wire calibration was conducted in an open-jet calibration facility in which a maximum calibration velocity of 45 m s^{-1} could be attained (the expected velocity at the downstream end of the contraction). The calibration consisted of constructing a look-up table for a range of velocities (0–45 m s^{-1}) and angles ($\pm 45°$, $\Delta = 1.8°$). The look-up table was constructed by least squares fitting surfaces to $Q(e_1, e_2)$ and $\alpha(e_1, e_2)$, where Q is the calibration velocity; α is the calibration angle; and e_1 and e_2 are the voltages of the X-wire sensors at the respective velocity and angle. Thus the measured voltages were transformed into velocity by the following method:

$$u_1(t) = Q(e_1, e_2, t)\cos(\alpha(e_1, e_2, t)), \tag{6.1}$$

$$u_2(t) = Q(e_1, e_2, t)\sin(\alpha(e_1, e_2, t)). \tag{6.2}$$

Each calibration had a unique look-up table which was processed prior to data acquisition and stored offline to optical media and a hard drive. A typical look-up table was constructed using 51 angles and 20 velocities in the aforementioned range. The relative uncertainty of the instantaneous velocity measured with the X-wire was determined to be ±2.0 % of the local mean velocity. Calibration was performed prior to each wind-tunnel run.

6.2. *Time-mean behaviour of the initial turbulent boundary layer*

In order to ensure the generality of the trends observed in this investigation, it is important to first characterize the 'initial' turbulent boundary layer prior to application of the streamwise acceleration and verify that it is canonical. The boundary layer mean velocity profile at $x/L = -2.58$, corresponding to $Re_\theta = 4600$, scaled in viscous wall units is shown in figure 3. Also shown for comparison are ZPG turbulent boundary layer mean velocity profiles measured by Österlund (1999) at $Re_\theta = 4613$, by Warnack as reported by Fernholz & Finley (1996) at $Re_\theta = 4736$ and by DeGraff & Eaton (2000) at $Re_\theta = 5200$. The measured profile at $x/L = -2.58$ is shown to be in good general agreement with the previous studies. The Kármán constant measured in the current study is $\kappa = 0.385 \pm 0.006$, and the additive constant is $B = 4.13$.

Figure 4(*a*) presents measurements of the mean-square streamwise fluctuating velocity in inner-variable scaling, obtained in the initial boundary layer at $x/L = -2.58$. Also plotted for comparison are the measurements by DeGraff & Eaton (2000) at $Re_\theta = 5200$, using a high-spatial-resolution laser Doppler anemometry (LDA) system, and by Warnack (see Fernholz & Finley 1996) at $Re_\theta = 4736$, using constant-temperature hot-wire anemometry. In each case, measurements show that peak values of $\langle u^2 \rangle / u_\tau^2$ occur near $y u_\tau / \nu = 15$. In the present study the peak value is approximately $\langle u^2 \rangle / u_\tau^2 = 7.75$, in good overall agreement with other studies at comparable Re_θ. The

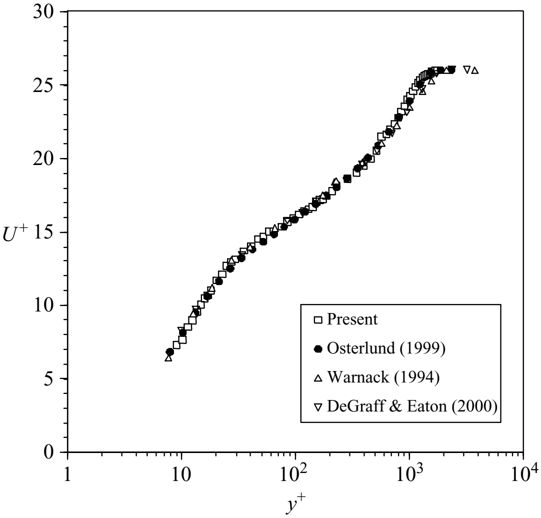

FIGURE 3. Inner-variable-scaled mean velocity profile at $x/L = -2.58$ compared with published profiles at comparable Re_θ.

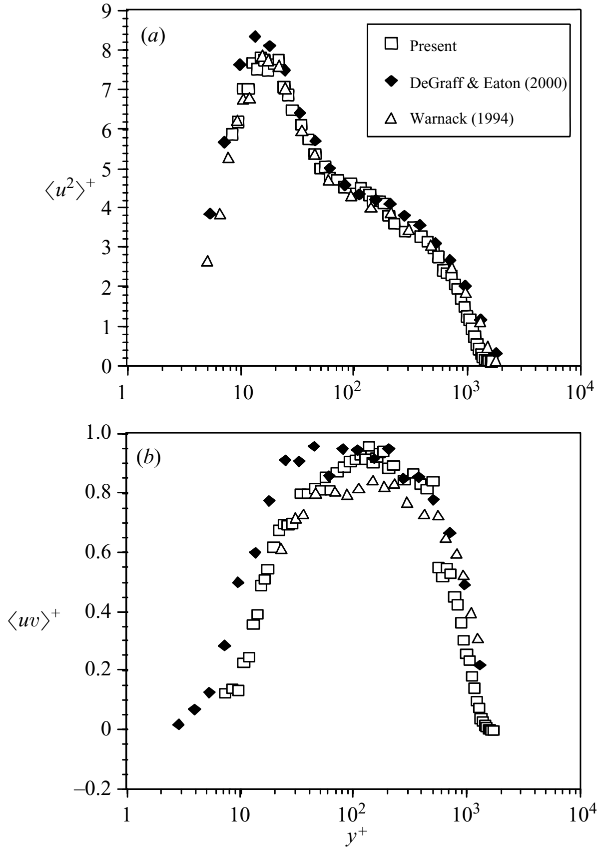

FIGURE 4. Profiles of (a) $\langle u^2 \rangle / u_\tau^2$ and (b) $-\langle uv \rangle / u_\tau^2$ for the ZPG turbulent boundary layer at $x/L = -2.58$. Shown for comparison are Warnack's (1994) and DeGraff & Eaton's (2000) turbulent boundary layer data.

measured Reynolds stress profile $-\langle uv\rangle/u_\tau^2$ at $x/L = -2.58$ is plotted in figure 4(*b*) along with corresponding measurements from the aforementioned references. While the Reynolds shear stress profiles are similar, it is noted that very near the wall the LDA-based measurements are consistently higher than in both experiments utilizing multi-sensor hot wires.

The mean flow and turbulence measurements presented in this section serve to demonstrate that the boundary layer upstream of the onset of flow acceleration exhibits canonical ZPG behaviour in good general agreement with previously published results.

7. Wall shear stress measurements

Significant departure of the mean velocity profiles from standard log-law behaviour was anticipated for the highly accelerated turbulent boundary layer under consideration in this investigation. For this reason, the wall shear stress could not be accurately determined using the Clauser or Preston tube methods. To avoid this difficulty, the wall shear stress was directly determined using the OFI technique. Implementation of the OFI technique involved application of silicone oil to a flush-mounted glass plate embedded in the wind-tunnel floor. Various viscosities of Dow Corning silicone oil were employed at different streamwise locations in order to account for the changing magnitude of the local mean shear. The oil was sheared for approximately 1 h for each run with a tunnel start-up time of approximately 1 min and a shut-down time of approximately 3 min. Once the oil was sheared, the glass plate was carefully removed from the wind tunnel for photography. An Osram SOX 55 watt low-pressure sodium lamp was used to illuminate the oil. The low-pressure sodium lamp was used for its characteristic light of wavelengths 589.0 nm and 589.6 nm, which eliminates the need for a special narrowband filter for the camera. An Olympus E10 digital camera with a resolution of 2240 × 1680 pixels was used to capture the interferograms. A fiduciary marker was placed next to the sheared oil for spatial reference, and the angle of the camera relative to the surface was recorded. Once the oil was illuminated and the camera was in position, several digital images were taken of each interferogram for post-processing.

The interferograms contain alternating bands of light and dark fringes resulting from interference between light reflected from the wind-tunnel (glass) floor and from the air–oil interface. The distance between two adjacent dark fringes is proportional to the local skin friction. A MATLAB graphical user interface (GUI) was developed for determining the skin friction from the interferograms. To identify fringes, the intensity of the interferograms was calculated, and the distance between peaks in the intensity plot was used to determine the fringe spacing. The relationship between fringe spacing and the skin friction was derived by Monson, Mateer & Menter (1993) and is given as

$$c_f = \frac{\left(\dfrac{2n\cos(\theta)\Delta}{\lambda}\right)}{\displaystyle\int_0^{t_{run}} \frac{q_\infty(t)}{\mu(t)}\,\mathrm{d}t}, \tag{7.1}$$

where n is the index of refraction of the silicone oil; θ is the refraction angle (assumed to be the angle of the camera relative to the wall-normal direction for this experiment); Δ is the fringe spacing; λ is the wavelength of the light; t_{run} is the total time the oil was sheared in the wind tunnel; $\mu(t)$ is the time-dependent viscosity; and

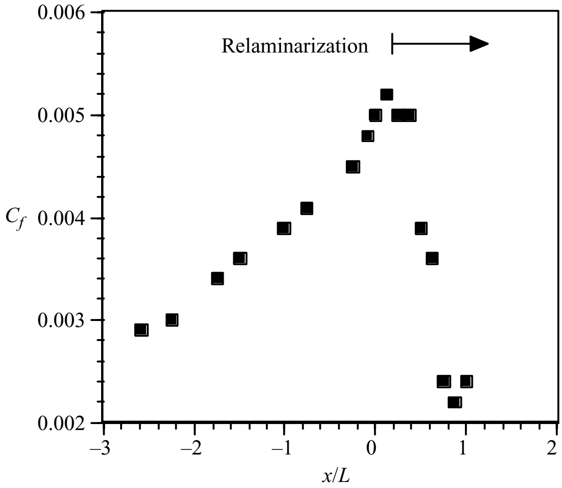

FIGURE 5. The skin friction coefficient evolution as measured using OFI.

$q_\infty(t)$ is the dynamic pressure recorded over the length of the wind-tunnel run. The integral of the ratio of dynamic pressure to viscosity is used to account for lengthy wind-tunnel start-up and shut-down times, where the transient shear present at the location of the oil is less than the steady state value. Generally, $\mu(t)$ is a function of time because the temperature of the wind-tunnel surface can change throughout the course of a run. However, unless large temperature changes are observed, it is often assumed that μ is constant over the period the oil is sheared, and this was certainly appropriate for this investigation. The history of the dynamic pressure was accounted for by sampling $q(t)$ at 1 kHz for a duration of 1 s at 10 s intervals. For each streamwise location, the wall shear stress was independently measured three times in order to ensure repeatability. The relative uncertainty of the OFI technique has been calculated to be approximately $\pm 6\,\%$ of the nominal computed value. For more information regarding the application of OFI in general, see Monson *et al.* (1993), Zilliac (1996, 1999) and Driver (1998).

Figure 5 presents the streamwise evolution of the skin friction coefficient c_f as measured by the OFI technique. For the initial ZPG boundary layer at $x/L = -2.58$ the value of $c_f = 0.0029$ is in excellent agreement with the Coles–Fernholz logarithmic skin friction relation (see Kapil, Nagib & Monkewitz 2005). In figure 5 the skin friction coefficient steadily increases from its ZPG value to a maximum value of $c_f = 0.0052$ at $x/L = 0.1$. Given the thinning of the turbulent boundary layer associated with the free-stream acceleration, this increase is expected. However, the skin friction coefficient rapidly decreases beyond $x/L = 0.1$ to a minimum value of $c_f = 0.0022$ at $x/L = 0.7$ and remains at this value through to the end of the contraction. This behaviour of the skin friction coefficient is a manifestation of relaminarization with the onset occurring near $x/L = 0.2$.

In order to verify the two-dimensionality of the flow field in the mean, a cross-stream integral momentum balance was performed based on local mean velocity profiles obtained using hot-wire anemometry. It is important to note that the skin friction calculated from the integral momentum balance showed excellent agreement with the direct OFI measurements shown in figure 5. In this manner the two-dimensionality of the mean flow field was clearly established in the region $-2.58 \leqslant x/L \leqslant 0.8$, which encompasses the region of the peak acceleration parameter.

$\delta_\circ$ (m)	$\delta_\circ^*$ (m)	$\theta_\circ$ (m)	$H_\circ$	Re_θ
0.145	0.021	0.015	1.37	4590

TABLE 2. ZPG reference values.

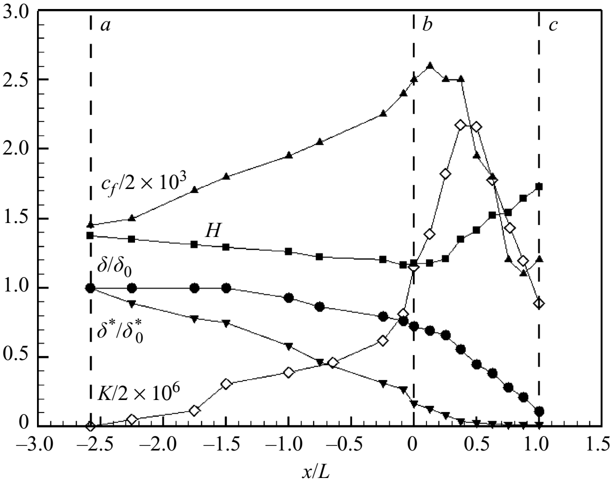

FIGURE 6. Streamwise evolution of selected boundary layer parameters.

8. Streamwise variation of global flow quantities

In order to characterize the streamwise evolution of the turbulent boundary layer, the development of measured global mean flow parameters is presented first. In particular, the streamwise development of the 99 % boundary layer thickness δ, the displacement thickness δ^*, the shape factor H and the local skin friction coefficient c_f are presented in figure 6. The boundary layer and displacement thicknesses in figure 6 are normalized by the initial ZPG values obtained at $x/L = -2.58$ (denoted with a subscript '$\circ$'). The reference values used to scale the global flow parameters are shown in table 2. Also shown in figure 6 is the acceleration parameter K, which reaches a maximum value of $K = 4.4 \times 10^{-6}$ for a streamwise interval inside the contraction of $\Delta x/L = 0.167$. Marked for reference in figure 6 are the x/L locations of the start of of the imposed free-stream acceleration (location a), the location of the beginning of the contraction (location b) and the location of the end of the contraction (location c). Figure 6 shows that the FPG upstream of the contraction has a significant effect on the boundary layer development even though the value of the acceleration parameter remains comparatively small. It must be noted, however, that although the K values in this region are modest in comparison to those encountered inside the contraction, the flow acceleration is still substantial. For example, over the range $-1.5 \leqslant x/L \leqslant 0$ the Clauser equilibrium parameter $\beta \equiv (\delta^*/\tau_w)\,\mathrm{d}P_e/\mathrm{d}x$ is nearly constant at a value of $\beta \approx -1.5$. Inside the contraction β increases linearly with x/L to reach a value of $\beta \approx -0.5$ at the exit. It is observed that both the boundary layer thickness and H decrease while c_f increases upstream of the contraction. Near the contraction inlet at which $K \approx 2.3 \times 10^{-6}$, H approaches a broad minimum value.

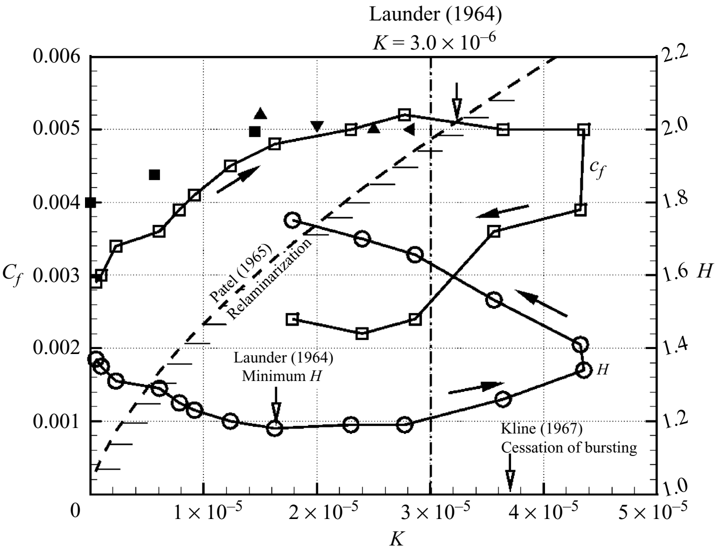

FIGURE 7. Development of the local skin friction c_f and shape factor H as a function of the acceleration parameter K. Arrows indicate streamwise development. Shown for reference are ▲, Jones & Launder (1972); ▼, Loyd, Moffat & Kays (1970); ◀, Badri Narayanan & Ramjee (1969); and ■, Julien, Kays & Moffat (1969).

Just inside the contraction inlet at $x/L = 0.125$ the skin friction reaches its maximum value corresponding to $K = 2.8 \times 10^{-6}$. As the boundary layer enters the contraction, the boundary layer thickness rapidly decreases, eventually reaching a value of only $\delta/\delta_o = 0.08$ by the end of the contraction. The initiation of the rapid reduction in boundary layer thickness and the precipitous drop in c_f corresponds to an acceleration parameter value of $K \approx 3.5 \times 10^{-6}$. The shape factor exhibits a sudden increase at this location, suggesting a major restructuring of the boundary layer mean velocity profile associated with the relaminarization process. This aspect will be examined in detail in the following section.

It is apparent that both the shape factor and the local skin friction coefficient are strongly influenced by the onset of the large FPG. Their relationship to the acceleration parameter can be more clearly seen by plotting each as a function of K, which is shown in figure 7. This figure also presents skin friction coefficient values reported in several previous studies (all at lower values of K). Figure 7 shows that the skin friction coefficient increases and the shape factor reaches a broad minimum just before $K = 3.0 \times 10^{-6}$ (indicated by a vertical line). The peak values of c_f observed in this investigation are in good general agreement with those obtained in previous studies. After $K \approx 3.0 \times 10^{-6}$ is exceeded, the skin friction coefficient begins to decrease, and the shape factor begins to increase. For $K > 4.0 \times 10^{-6}$, a very rapid drop in the skin friction coefficient is observed, and this drop is associated with a greater rate of increase in the shape factor. This behaviour is sustained even after K begins to decrease from its maximum value.

Also shown in figure 7 are several previously proposed indicators of relaminarization. With the exception of the minimum H criterion of Launder (1964), all indicate relaminarization locations either at or just downstream of the observed initial reduction in c_f. The $\Delta p = -0.025$ criterion proposed by Patel (1965) is equivalently represented in figure 7 by requiring

$$0.025 = K\left(\frac{2}{c_f}\right)^{\frac{3}{2}}. \tag{8.1}$$

The intersection of this curve with the measured skin friction coefficient defines the location $\Delta p = -0.025$ for the current experiment. This is observed to correspond to a streamwise location just downstream of $K \approx 3.2 \times 10^{-6}$ and near the onset of the observed reduction of c_f. The K value associated with cessation of bursting as observed by Kline *et al.* (1967) occurs upstream of the sudden reduction of c_f observed in the current experiment. With perhaps the exception of the shape factor, it is evident from figure 7 that the response of the skin friction to the streamwise flow acceleration is reasonably correlated with each of the indicators of relaminarization.

The parameter $\Gamma(x) = (-\mathrm{d}p/\mathrm{d}x)\delta(x)/\tau_w$ provides a local measure of the ratio of the streamwise pressure gradient to the cross-stream stress gradient. Narasimha & Sreenivasan (1973) refer to this quantity as the 'pressure gradient' parameter. Unable to measure skin friction in their highly accelerated boundary layer, Narasimha & Sreenivasan (1973) assumed frozen Reynolds stress and argued that the wall shear stress at the start of the large FPG, $\tau_w(x_\circ)$, is representative of the Reynolds stress in the accelerated boundary layer downstream. Narasimha & Sreenivasan (1973) observed a value of $\Gamma(x) = 50$ to coincide with relaminarization, which occurred downstream of the location at which $K = 3.0 \times 10^{-6}$. In the current experiment the streamwise variation of $\Gamma(x) = (-\mathrm{d}p/\mathrm{d}x)\delta(x)/\tau_w$ was obtained by using local values of τ_w from the OFI measurement. It is found that the initial reduction in skin friction and associated increase in shape factor occurs for $\Gamma(x) = 300$, while $K = 3.0 \times 10^{-6}$ corresponds to $\Gamma(x) \approx 500$. Thus when the ratio of the local pressure gradient to the stress gradient is approximately 300, the boundary layer begins to show behaviour consistent with onset of relaminarization. The more sudden decrease in skin friction coefficient that occurs downstream corresponds to the much higher value of $\Gamma(x) \approx 2750$. These values reflect the dominance of streamwise pressure gradient in relation to the local stress gradient in the current experiment.

9. Mean velocity profiles

In this section the distortion of the boundary layer mean velocity profiles in response to the imposed FPG is described.

Alternatives to the classical Clauser–Millikan logarithmic law of the wall have recently been proposed for the scaling of the turbulent boundary layer mean velocity. These include the 'near asymptotics' approach of George & Castillo (1997) and George (2006) in which the free-stream velocity rather than the friction velocity is chosen as the outer velocity scale. This approach leads to a power-law representation of the mean velocity in the overlap region. Power-law theories have also been developed by Barenblatt (1993), Baranblatt, Chorin & Prostokishin (2000) and Oberlack (2001). However, in a recent comprehensive evaluation of turbulent boundary layer similarity laws by Monkewitz, Chauhan & Nagib (2008) based on a common set of 300 mean velocity profiles from 20 different ZPG boundary layer experiments, the superiority of the classical logarithmic law for ZPG turbulent boundary layers is now clearly established. In the absence of a comprehensive theory for non-equilibrium FPG turbulent boundary layers, we employ the classic Kármán–Millikan–Rotta–Clauser scaling in the evaluation of the mean velocity profiles obtained in this study. This

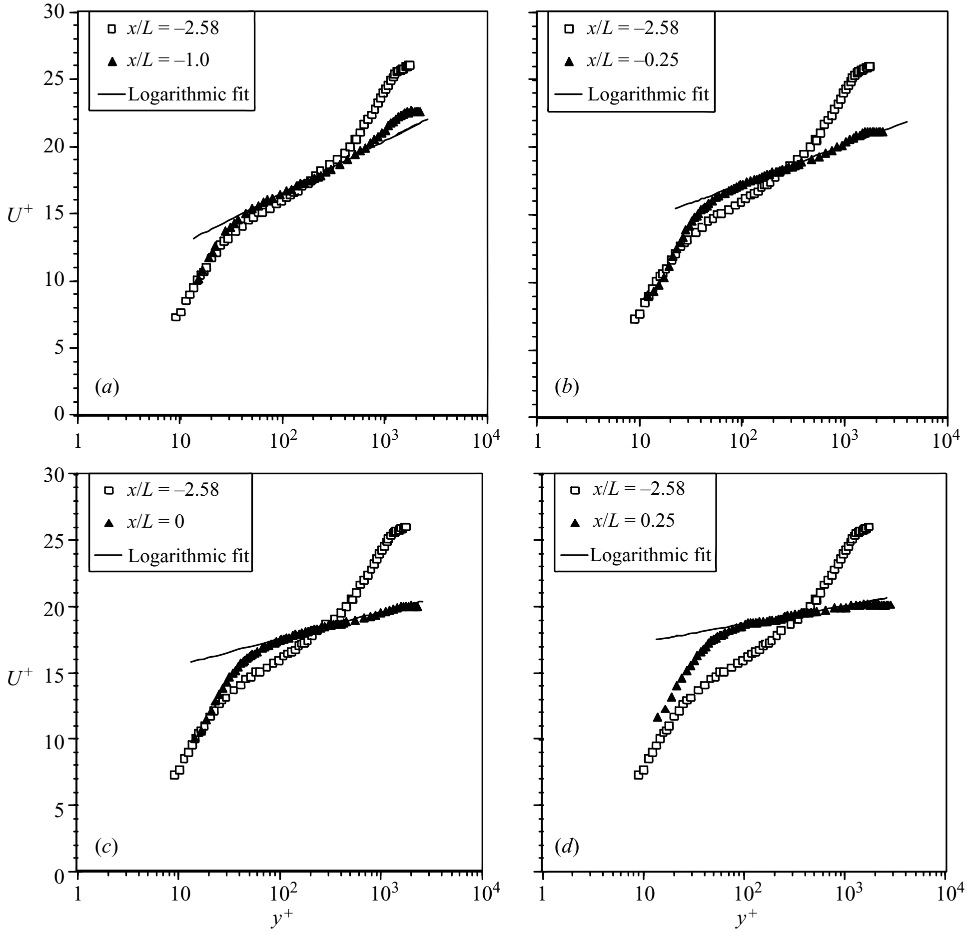

FIGURE 8. Mean velocity profiles in inner-variable scaling at representative streamwise locations: (*a*) $x/L = -1.0$, (*b*) $x/L = -0.25$, (*c*) $x/L = 0.0$, (*d*) $x/L = 0.25$.

approach facilitates a meaningful comparison with previous experiments in sink-flow FPG boundary layers, which have also employed the classical logarithmic scaling.

Sample inner-variable-scaled mean velocity profiles in the range $-1.0 \leqslant x/L \leqslant 0.25$ (representing locations both upstream and inside the internal contraction; see figure 6) are plotted in figure 8. In each case the $x/L = -2.58$ mean velocity profile corresponding to ZPG is shown for comparison with the FPG boundary layer profiles measured at $x/L = -1.0$, –0.25, 0 and 0.25, the last location being just inside the region of relaminarization. The influence of the FPG in distorting the local mean velocity profiles from that at $x/L = -2.58$ is readily apparent. Two aspects in particular should be noted; the first is the complete loss of the outer wake region, and the the second is the persistence of a logarithmic region. For the logarithmic region it will be shown that there is a systematic deviation from standard values of the slope (i.e. $1/\kappa$) and additive constant B.

A systematic procedure was utilized for establishing the region of logarithmic variation for each measured boundary layer mean velocity profile. This involves first establishing the range of y^+ values for which the diagnostic function $\Xi = y^+ \mathrm{d}u^+/\mathrm{d}y^+$ is effectively constant. A representative example is shown in figure 9. This figure shows

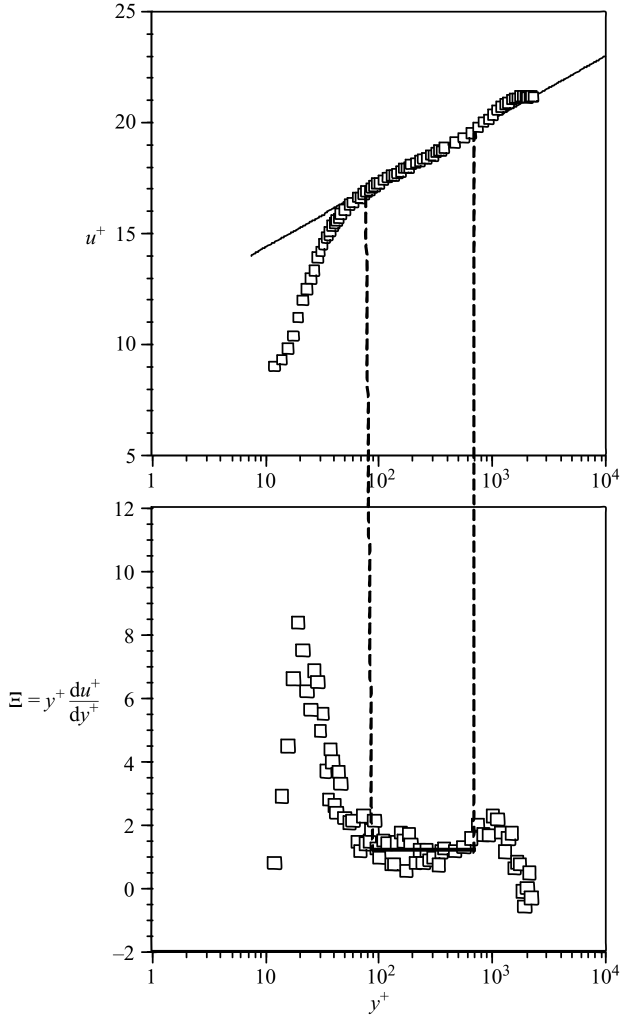

FIGURE 9. Sample diagnostic function and inner-variable-scaled mean velocity at $x/L = -0.25$.

the diagnostic function and corresponding inner-variable-scaled mean velocity profile for the streamwise location of $x/L = -0.25$ which corresponds to a relatively strong flow acceleration of $K = 1.23 \times 10^{-6}$. The region of the profile exhibiting logarithmic variation is clearly indicated. Similarly, at each streamwise location investigated, the diagnostic function Ξ revealed that a portion of the local boundary layer mean velocity profile exhibits a region of logarithmic variation. In order to establish the local logarithmic fit to very high statistical certainty, requirements were placed on the number of data points N (i.e. measured u^+, y^+ pairs) within the region and on the value of the associated correlation coefficient r. In this study the logarithmic fit at each x/L station was based upon the constraints that $N \geqslant 25$ and $r \geqslant 0.98$. By using standard statistical methods like those presented in Dunn (2005), one can show that with the stated constraints on N and r, the probability that the mean velocity *does not* exhibit a logarithmic variation in the region is insignificant (less than 0.001 %).

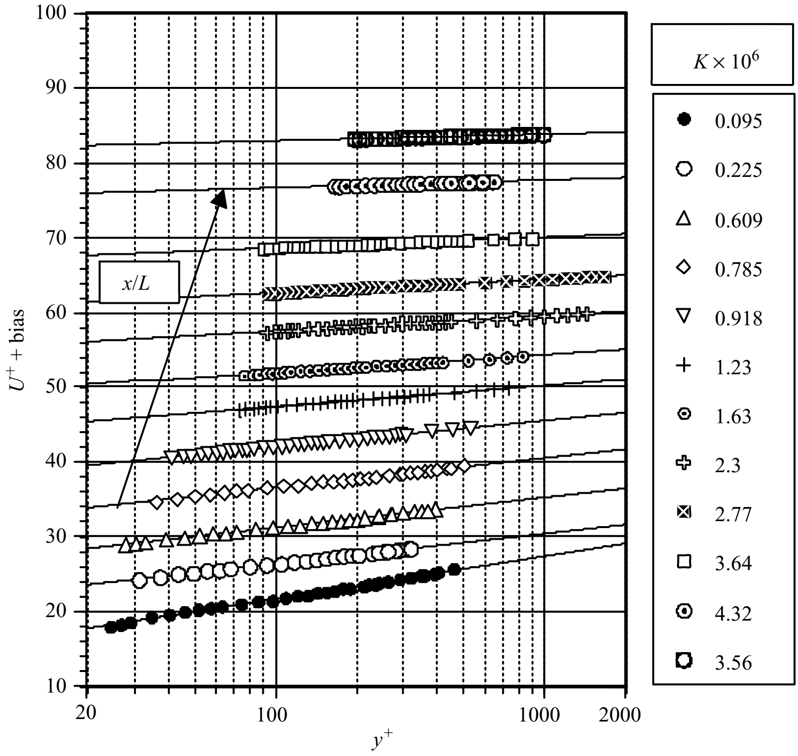

FIGURE 10. Effect of the local value of the acceleration parameter K on the logarithmic region of the mean velocity profile.

For each profile shown in figure 8, a logarithmic region exists for some range of yu_τ/ν based on the aforementioned statistical requirements and is also shown at each x/L location. Note that the degree of deviation from standard logarithmic behaviour increases with the acceleration parameter. Similar mean velocity profile distortion for accelerated turbulent boundary layers is also apparent from the mean velocity measurements shown in figure 5 of Blackwelder & Kovasznay (1972) and in figure 6 of Narasimha & Sreenivasan (1973) and more recently from the sink-flow turbulent boundary layer measurements shown in figure 8 of Dixit & Ramesh (2008). In addition to preserving a region of logarithmic variation, the profiles of figure 8 also suggest a thickening of the buffer and laminar sublayers.

For representative locations nearing relaminarization in figure 8(c, d) the deviation from the standard log law is obviously quite substantial, and the outer wake region of the profile is totally absent. However, even for the high flow acceleration encountered inside the contraction, a well-defined logarithmic region still exists. The slope of the logarithmic region is found to vary systematically with x/L, and this is clearly demonstrated in figure 10 which highlights the logarithmic region of several mean velocity profiles as well as the local logarithmic fit. In order to better demonstrate the trends, each profile is given a bias of $u^+ = 5$ from the profile immediately upstream. In each case, the local value of the acceleration parameter K is given. It is clear from this figure that there is a systematic reduction in the slope of the logarithmic region with increased K. It is also apparent that the logarithmic region commences farther from the wall and extends over a smaller range of yu_τ/ν values as K increases.

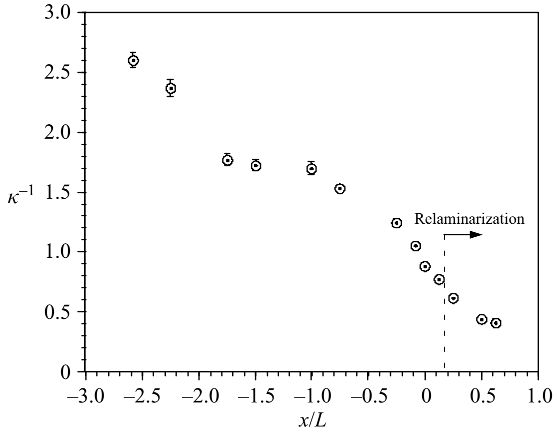

FIGURE 11. Variation of κ^{-1} with x/L.

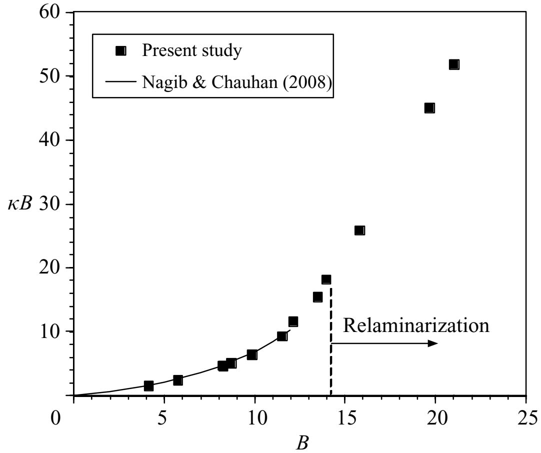

FIGURE 12. Variation of κB with additive constant B.

In figure 11 the variation of κ^{-1} with the streamwise coordinate x/L is presented along with 95 % confidence intervals. The region of boundary layer relaminarization is indicated, and it may be noted that κ^{-1} varies smoothly as the flow undergoes relaminarization. Morrison, Subramanian & Bradshaw (1992) noted that κ^{-1} may be interpreted as the efficiency with which ejections or sweeps transport momentum. If this is indeed the case, then figure 11 suggests a reduction in efficiency with which burst/sweep events transport momentum with respect to the active flow as the boundary layer is exposed to the streamwise acceleration. This aspect is further explored via conditional measurements presented later in this paper.

Figure 12 presents the product of the logarithmic law parameters κ and B as a function of the additive constant B. In this figure higher values of K proceed from left to right (i.e. with increasing B), and the region of relaminarization is indicated. This figure clearly demonstrates that κ and B are *both* well correlated with the imposed flow acceleration and are not just arbitrary constants used to fit the overlap region. In a recent paper Nagib & Chauhan (2008) demonstrated that the Kármán constant is not universal but exhibits a dependence on both flow geometry and

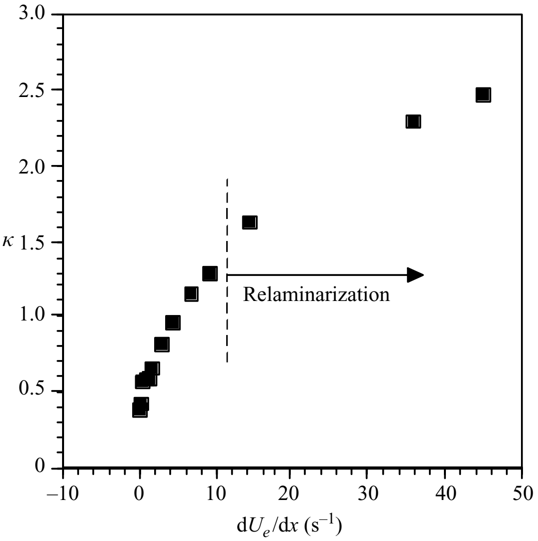

FIGURE 13. Variaton in the Kármán constant with longitudinal strain rate, dU_e/dx.

pressure gradient. They demonstrate the coherence of κB as a function of B for a wide range of boundary layer data involving both FPG and adverse pressure gradient (APG). They proposed the empirical fit $\kappa B = 1.6[\exp(0.1663B) - 1]$ to this large body of experimental results, which is denoted by the solid curve shown in figure 12. Results from the current experiment are found to be in excellent agreement with the correlation by Nagib & Chauhan (2008) and also smoothly extend the data set to much larger values of κB and B, leading to relaminarization. The interested reader will also find values of κ and B from the current study plotted in figure 5 of Nagib & Chauhan (2008). These data were added to the original version of the figure which appeared in the thesis by Chauhan (2007).

Figure 13 presents the measured values of the Kármán constant as a function of the applied longitudinal strain rate, $dU_e/dx = U_e^2 K/\nu$. It is clear that there is a systematic variation of κ with the applied strain rate. Note that the change in the Kármán constant is not associated with onset of relaminarization; significant variations occur upstream of onset, and κ varies smoothly with strain rate through the onset of relaminarization. It is also interesting to note that the sensitivity of the Kármán constant to longitudinal strain rate is actually greatest for very small strain rates. This may explain, in part, the variation in reported values for the Kármán constant due to ZPG boundary layer experiments that are actually (but unintentionally) performed in small FPGs.

The variation of the Kármán constant as a function of the spatial gradient of longitudinal strain, $(1/U_e)\, dU_e/dx$, is presented in figure 14. This figure shows that for FPG below that giving rise to relaminarization, κ is, to good approximation, proportional to the spatial longitudinal strain gradient.

The local wall-normal location at which the boundary layer mean velocity profile first shows evidence of log-law behaviour in inner-variable scaling is denoted y_0^+ and is plotted as a function of streamwise position x/L in figure 15. This figure shows that, despite the considerable thinning of the boundary layer as a whole, the combined thicknesses of the viscous sublayer and the buffer layer grow significantly upon encountering the large flow acceleration upstream and inside the contraction

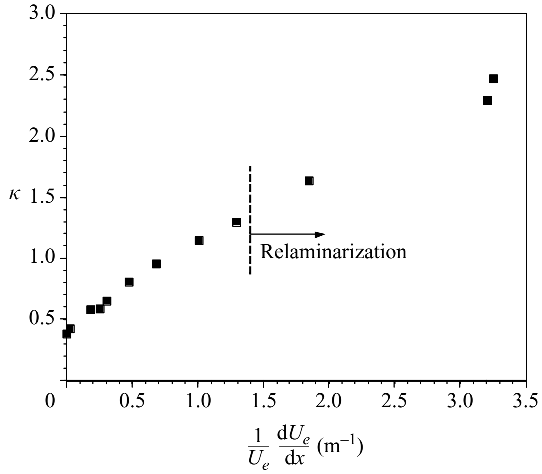

FIGURE 14. Variaton in the Kármán constant with the spatial gradient of longitudinal strain, $(1/U_e)\,dU_e/dx$.

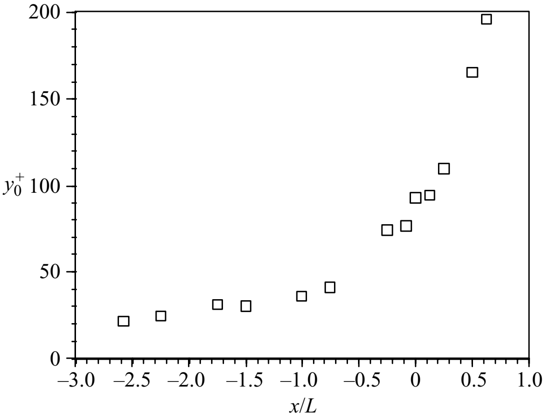

FIGURE 15. Streamwise variation in thickness of the viscous wall region, y_0^+.

inlet. The increase in viscous wall layer thickness associated with relaminarization inside the contraction is particularly dramatic.

It is of interest to compare mean flow results from the current investigation with those involving turbulent boundary layer sink flow. The sink flow is unique in the sense that it is the only smooth wall turbulent boundary layer flow that precisely satisfies the conditions for dynamic equilibrium. Because of this, the flow takes on a form independent of streamwise location, and any Reynolds number based on local velocity and length scales is constant. Further, while the local pressure gradient plays a role in the equilibrium sink-flow boundary layer, pressure gradient history effects are absent. In contrast, the current experiment involves a highly non-equilibrium FPG flow in which both local pressure gradient and pressure gradient history influence the streamwise evolution of the flow.

Jones, Marusic & Perry (2001) reported a careful set of boundary layer measurements obtained under FPG conditions corresponding to sink flow. Their largest value of acceleration parameter is $K = 5.39 \times 10^{-7}$. More recently, Dixit &

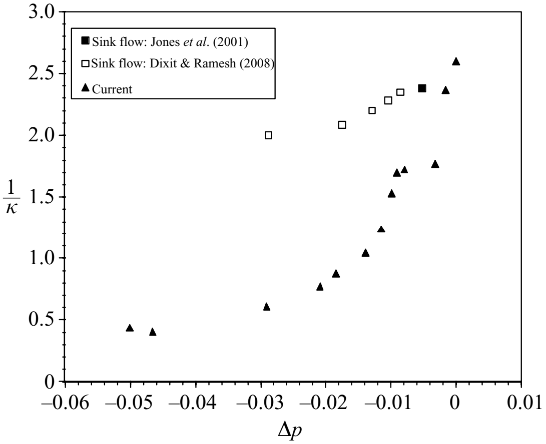

FIGURE 16. Comparison of the variation of $1/\kappa$ with Δp for sink-flow turbulent boundary layers and the current non-equilibrium experiment.

Ramesh (2008) reported the results of five experiments in sink-flow turbulent boundary layers with the largest value of the acceleration parameter $K = 2.9 \times 10^{-6}$. Figure 16 presents measurements of the slope of the logarithmic profile, $1/\kappa$, as a function of the pressure gradient parameter Δp defined in (2.2). This figure contains results from Jones *et al.* (2001), for their largest value of K, as well as the five experiments of Dixit & Ramesh (2008). These are compared with measurements of $1/\kappa$ from the current study. Figure 16 shows that in both the sink-flow boundary layers and the current study, $\mathrm{d}(1/\kappa)/\mathrm{d}(\Delta p) > 0$. Dixit & Ramesh (2008) offered a heuristic argument for the observed variation of $1/\kappa$ with pressure gradient. They noted that turbulence production is generally attenuated in FPG boundary layers, so that $\mathrm{d}P^+/\mathrm{d}(\Delta p) > 0$, where $P^+ = -\langle uv\rangle/u_\tau^2(\mathrm{d}u^+/\mathrm{d}y^+)$. Since $-\langle uv\rangle/u_\tau^2 \sim O(1)$ it follows that $\mathrm{d}(\mathrm{d}u^+/\mathrm{d}y^+)\mathrm{d}(\Delta p) > 0$ which, in the overlap region, requires $\mathrm{d}(1/\kappa)/\ d(\Delta p) > 0$. It is important to remember that each of the sink-flow datum points presented in figure 16 corresponds to a separate equilibrium boundary layer experiment. In contrast, the results from the current study represent the variation of $1/\kappa$ with Δp as the flow evolves spatially. The difference between the equilibrium and non-equilibrium flows shown in figure 16 is likely an indication of the importance of pressure gradient history effects in the current experiment.

10. Evolution of turbulence quantities

10.1. *Evolution of mean-square fluctuations*

In this section the streamwise development of the boundary layer turbulent stresses are presented. Consideration is first given to the effect of favourable streamwise pressure gradient on the mean-square streamwise fluctuating velocity component $\langle u^2\rangle$. The first point to be made is that $\langle u^2\rangle$ exhibits a dual-layer response to the external flow acceleration. For wall-normal locations below $yu_\tau/\nu \approx 100$, $\langle u^2\rangle$ exhibits growth with x/L. In contrast, $\langle u^2\rangle$ gradually decays with streamwise distance over the largest wall-normal extent of the boundary layer ($yu_\tau/\nu > 100$). This can be clearly seen by examining figure 17 which presents cross-stream profiles of the ratio of local $\langle u^2\rangle$ to that measured upstream for the initial ZPG boundary layer at $x/L = -2.58$ (denoted $\langle u_0^2\rangle$). Two representative profiles are shown: one obtained just upstream of

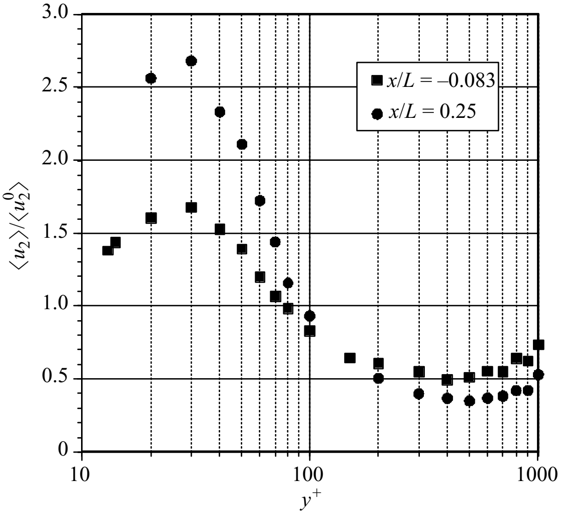

FIGURE 17. Streamwise development of $\langle u^2 \rangle / \langle u_0^2 \rangle$.

the contraction and the other inside where the boundary layer relaminarizes. It may be observed that $yu_\tau/\nu \approx 150$ delineates an approximate boundary between wall-normal locations, showing streamwise growth and decay of $\langle u^2 \rangle$.

Figure 18(a, b) presents profiles of $\langle u^2 \rangle / u_\tau^2$ for selected streamwise locations both upstream and inside the contraction, respectively. In each case, the abscissa presents the wall-normal coordinate in inner-variable scaling. It is apparent from profiles upstream of the contraction that $\langle u^2 \rangle / u_\tau^2$ decreases with x/L over virtually the entire extent of the boundary layer. The greatest reduction occurs in the outer portion of the boundary layer, and this is a consequence of decaying $\langle u^2 \rangle$ normalized with an increasing friction velocity. Closer to the wall at which $\langle u^2 \rangle$ exhibits growth, the peak value of $\langle u^2 \rangle / u_\tau^2$ decreases with x/L, indicating that the normal stresses do not scale with u_τ. Note also that the near-wall peak in the the $\langle u^2 \rangle / u_\tau^2$ profile shifts from $yu_\tau/\nu = 15$ to $yu_\tau/\nu = 23$ as the flow is accelerated. In contrast, for those locations inside the contraction that are associated with relaminarization, profiles of $\langle u^2 \rangle / u_\tau^2$ exhibit a reasonable collapse, indicating that in the region of largest K the near-wall growth in $\langle u^2 \rangle$ scales with friction velocity. Figure 18(b) shows that peak values of $\langle u^2 \rangle / u_\tau^2 \approx 3.6$ near $yu_\tau/\nu \approx 23$; a 54 % reduction from the corresponding ZPG value.

Figure 19(a, b) shows representative cross-stream profiles of $\langle v^2 \rangle / u_\tau^2$ for selected x/L locations upstream and inside of the contraction, respectively. Figure 19(a) shows that $\langle v^2 \rangle / u_\tau^2$ decreases with x/L over most of the wall-normal extent of the boundary layer. However, for $yu_\tau/\nu < 30$ a reasonable collapse is obtained for an intermediate range of x/L values upstream of the contraction, which are associated with comparatively small values of K. Inside the contraction, $\langle v^2 \rangle / u_\tau^2$ continues to decrease with x/L for $yu_\tau/\nu > 30$. In the near-wall region, however, $\langle v^2 \rangle / u_\tau^2$ exhibits streamwise growth with peak values centred near $yu_\tau/\nu \approx 20$. For streamwise locations associated with relaminarization, the near-wall peak scales with u_τ and $\langle v^2 \rangle / u_\tau^2 \approx 0.7$. This peak value is approximately 40 % greater than at the same yu_τ/ν location near the contraction inlet, indicating increasingly vigorous $\langle v^2 \rangle$ levels near the wall relative to u_τ for the streamwise locations associated with relaminarization.

Although not presented here, profiles of $\langle w^2 \rangle / u_\tau^2$ show that $\langle w^2 \rangle / u_\tau^2$ decreases throughout the boundary layer in response to the applied FPG. Only for x/L stations

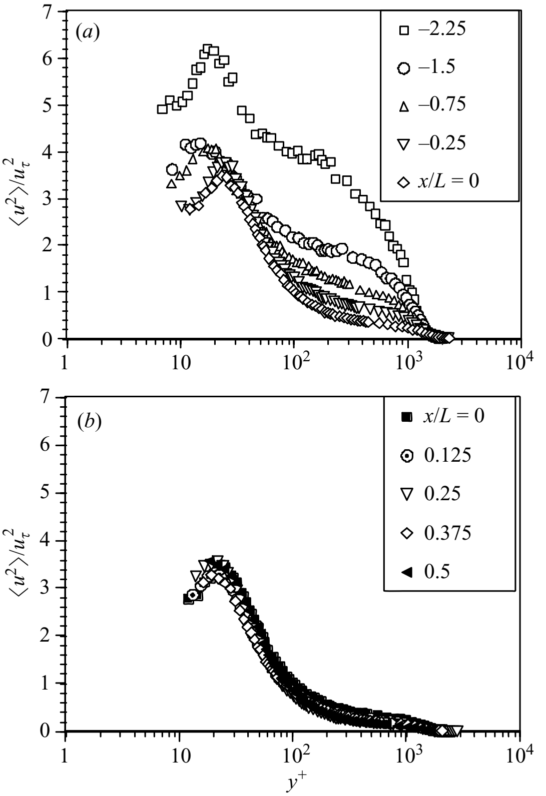

FIGURE 18. Streamwise development of $\langle u^2\rangle/u_\tau^2$ (*a*) upstream of the contraction and (*b*) downstream of the contraction.

inside the contraction do the profiles approach some level of collapse. Examination of unscaled profiles of $\langle w^2\rangle$ reveals that there is little streamwise variation of the profiles for x/L upstream of the contraction inlet. Hence the reduction in $\langle w^2\rangle/u_\tau^2$ levels is largely due to the increase in friction velocity with x/L. Inside the contraction,$\langle w^2\rangle$ levels increase, with the highest values occurring in the near-wall region of the boundary layer. This increase in $\langle w^2\rangle$ does not fully scale with the local friction velocity, however.

Inner-variable-scaled profiles of turbulent kinetic energy k/u_τ^2 versus yu_τ/ν are plotted in figure 20, where $k\equiv(1/2)\langle u_iu_i\rangle$. This figure reveals that the profiles of k/u_τ^2 do not scale upstream of the contraction inlet; turbulent kinetic energy clearly decreases in relation to the local value of u_τ^2. However, for the larger flow acceleration encountered inside the contraction which is associated with relaminarization, profiles of k/u_τ^2 exhibit a reasonable collapse with peak values of $k/u_\tau^2\approx 2.2$ occurring at $yu_\tau/\nu\approx 20$.

The ratios of mean-square velocities, $\langle u^2\rangle/\langle v^2\rangle$, $\langle u^2\rangle/\langle w^2\rangle$ and $\langle w^2\rangle/\langle v^2\rangle$, are plotted in figure 21(*a–c*), respectively. Figure 21(*a*) presents profiles of $\langle u^2\rangle/\langle v^2\rangle$ at representative x/L locations both upstream and inside the contraction. This figure clearly shows that the boundary layer acceleration gives rise to a reduction in $\langle u^2\rangle/\langle v^2\rangle$ in the near-wall region. That is near-wall v-component fluctuations grow in relation to u-fluctuations as the boundary layer accelerates. As expected, $\langle u^2\rangle/\langle v^2\rangle\rightarrow 1$ near the outer edge of the boundary layer.

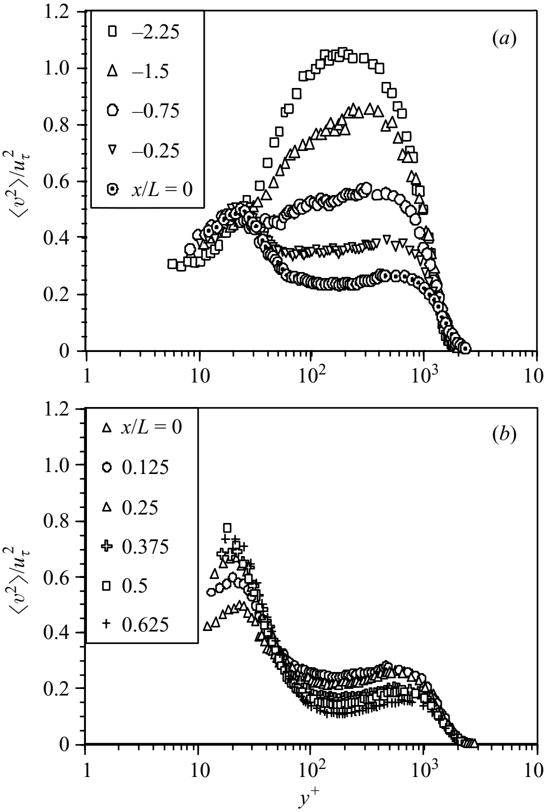

FIGURE 19. Streamwise development of $\langle v^2 \rangle / u_\tau^2$ (*a*) upstream of the contraction and (*b*) downstream of the contraction.

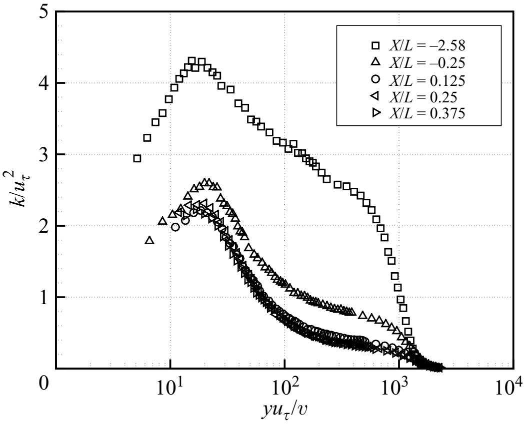

FIGURE 20. Streamwise development of inner-variable-scaled turbulent kinetic energy k/u_τ^2.

In figure 21(*b*), the ratio of $\langle u^2 \rangle / \langle w^2 \rangle$ is plotted for the accelerated boundary layer. The main feature to note is a progressive increase in $\langle u^2 \rangle / \langle w^2 \rangle$ in the region below $yu_\tau/\nu \approx 200$. A well-defined peak is evident whose value exhibits a nearly fivefold increase with x/L and whose distance from the wall progressively increases. Above $yu_\tau/\nu = 200$, the ratio $\langle u^2 \rangle / \langle w^2 \rangle$ exhibits comparatively little variation with

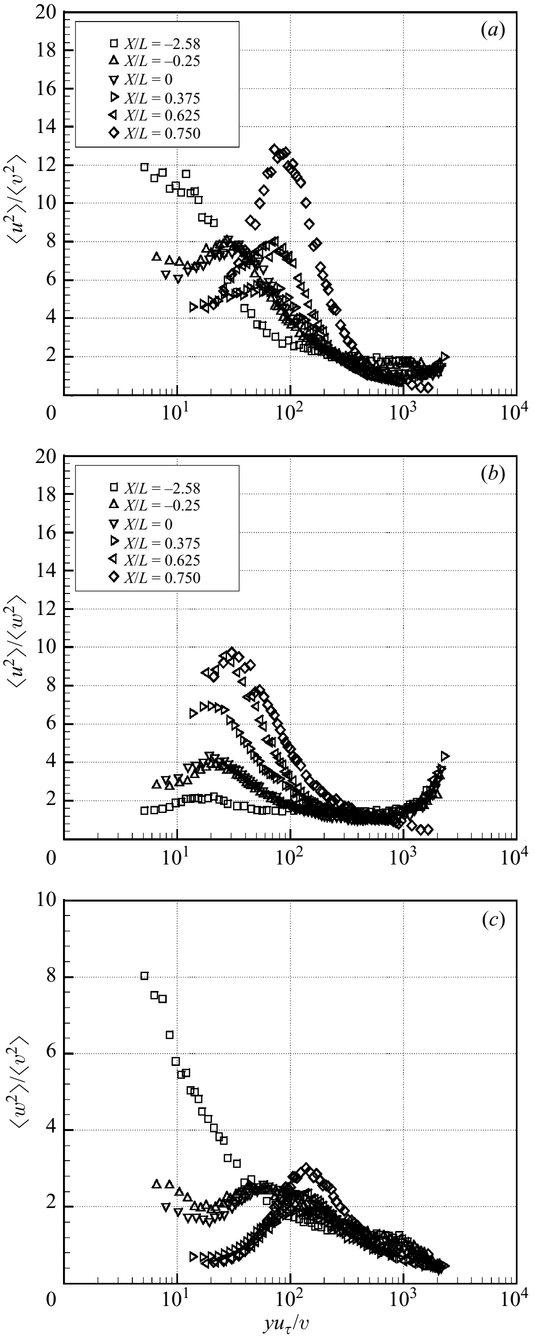

FIGURE 21. Streamwise development of the ratio of fluctuating velocities versus yu_τ/ν: (*a*) $\langle u^2\rangle/\langle v^2\rangle$, (*b*) $\langle u^2\rangle/\langle w^2\rangle$ and (*c*) $\langle w^2\rangle/\langle v^2\rangle$.

x/L. As the edge of the boundary layer is approached, $\langle u^2\rangle/\langle w^2\rangle$ increases, and the profiles exhibit collapse for all streamwise locations. Warnack & Fernholz (1998 *b*) also observed an increase in the ratio of $\langle u^2\rangle/\langle w^2\rangle$ in the near-wall region. Although not evident in figure 21(*b*), a peak in $\sqrt{(\langle w^2\rangle/\langle u^2\rangle}$ develops at $yu_\tau/\nu \approx 500$ with a

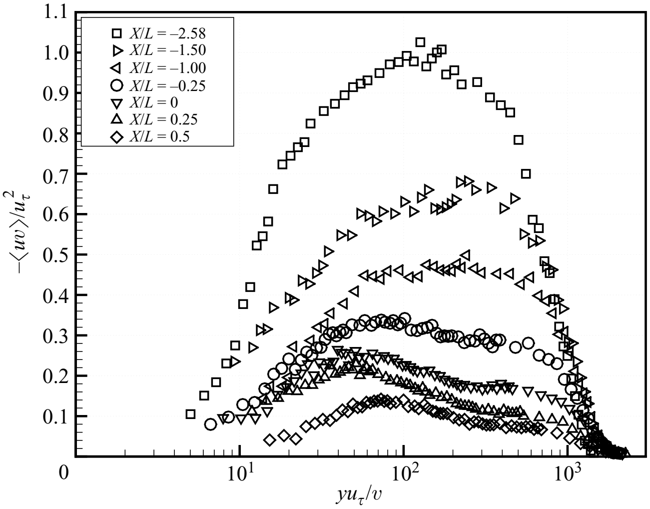

FIGURE 22. Streamwise evolution of the Reynolds stress normalized by the friction velocity.

maximum value of $\sqrt{(\langle w^2\rangle/\langle u^2\rangle)} = 1.05$ at $x/L = 0.25$, corresponding to $Re_\theta = 500$. In a similar fashion, Warnack & Fernholz (1998*b*) recorded a peak value of $\sqrt{(\langle w^2\rangle/\langle u^2\rangle)} = 1.35$ at $yu_\tau/\nu \approx 500$ corresponding to $Re_\theta = 420$.

In figure 21(*c*), the ratio of $\langle w^2\rangle/\langle v^2\rangle$ is shown. A large progressive reduction in the ratio is apparent in the near-wall region below $yu_\tau/\nu = 100$. For locations inside the contraction a peak develops in the range $100 < yu_\tau/\nu < 200$, whose value grows with x/L. It is interesting to note that the wall-normal location of the peak corresponds approximately to the thickness y_o^+ of the combined viscous sublayer and buffer regions denoted in previously in figure 15.

11. Reynolds shear stress

Consideration is next given to the response of the boundary layer Reynolds shear stress to the imposed external flow acceleration. The streamwise evolution of Reynolds stress profiles scaled by the square of the local friction velocity (as derived from the OFI measurements) is plotted in figure 22. The wall-normal coordinate is expressed in inner-variable scaling. Profiles of $-\langle uv\rangle/u_\tau^2$ are shown over a representative range of x/L locations both upstream and inside of the contraction. Since $-\langle uv\rangle/u_\tau^2$ is equivalent to $-\rho\langle uv\rangle/\tau_w$, these profiles provide a direct comparison between the boundary layer Reynolds stress and local wall shear stress.

From figure 22 it is apparent that as the boundary layer is accelerated, the Reynolds shear stress diminishes in relation to the local wall shear stress. Only for the most upstream measurement locations of $x/L = -2.58, -2.25$ (which are associated with comparatively small values of K) is there a constant stress region with $-\langle uv\rangle/u_\tau^2 \approx 1.0$. In contrast, for the largest values of K encountered in the experiment, the values of $-\langle uv\rangle/u_\tau^2$ are observed to become quite small.

An alternate measure of the response of the Reynolds shear stress to the external flow acceleration is the Reynolds stress correlation coefficient $-\langle uv\rangle/\langle u^2\rangle^{1/2}\langle v^2\rangle^{1/2}$. In effect, this allows one to assess the influence of the flow acceleration on the time-mean phase relationship between u- and v-component boundary layer velocity fluctuations. Reynolds stress correlation coefficient profiles are presented for a representative

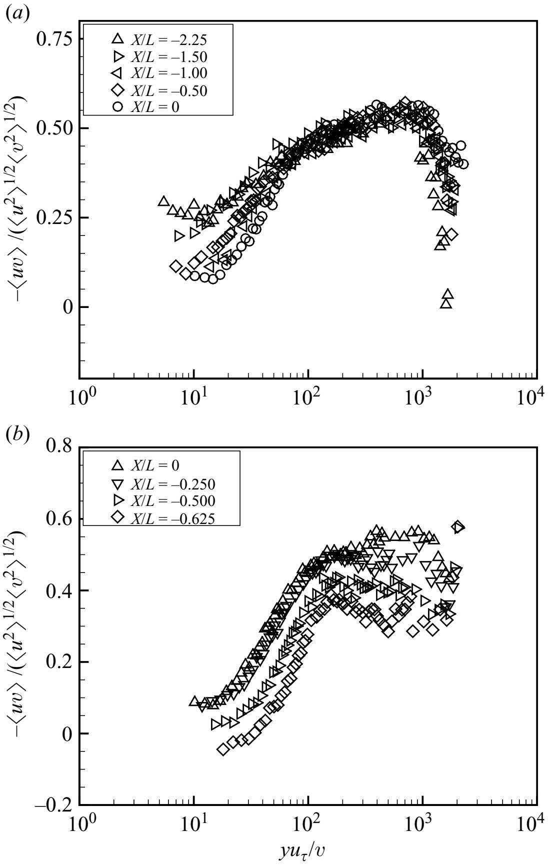

FIGURE 23. Streamwise evolution of the Reynolds stress correlation coefficient $-\langle uv\rangle/\langle u^2\rangle^{1/2}\langle v^2\rangle^{1/2}$ versus yu_τ/ν: (*a*) $x/L < 0$, (*b*) $0 \leqslant x/L \leqslant 0.625$.

range of x/L in figure 23. The correlation coefficient reaches a nearly constant value in the boundary layer for wall-normal locations $200 \leqslant yu_\tau/\nu \leqslant 1200$. Upstream of the imposed flow acceleration the correlation coefficient is 0.46 which compares well with the corresponding values of 0.44 and 0.5 measured by Lu & Willmarth (1973) and Klebanoff (1955), respectively. This value is also consistent with those at comparable Re_θ presented in figure 6 of Adrian, Meinhart & Tomkins (2000). For streamwise locations upstream of the contraction, the effect of the comparatively mild flow acceleration is to increase the values of $-\langle uv\rangle/\langle u^2\rangle^{1/2}\langle v^2\rangle^{1/2}$ for these wall-normal positions. The streamwise increase ranges from approximately 0.46 to nearly 0.6. In contrast, the flow acceleration is found to significantly reduce the correlation coefficient for wall-normal locations $yu_\tau/\nu < 100$. This reduction first becomes apparent near $x/L \approx -1.0$ which corresponds to $K \approx 0.7 \times 10^{-6}$. For the severer flow acceleration encountered inside the contraction, $-\langle uv\rangle/\langle u^2\rangle^{1/2}\langle v^2\rangle^{1/2}$ decreases for all wall-normal positions. The values near the wall are found to be particularly low. In fact, for streamwise locations associated with relaminarization, the correlation coefficient approaches zero in the near-wall region. The values of $-\langle uv\rangle/\langle u^2\rangle^{1/2}\langle v^2\rangle^{1/2}$ increase with distance from the wall, but even in the outer portion of the boundary layer they remain lower than at corresponding yu_τ/ν positions upstream of the contraction.

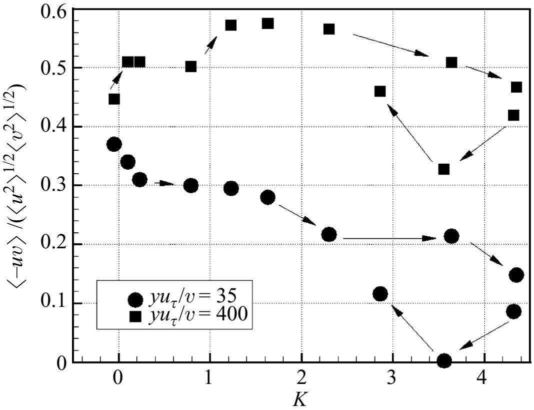

FIGURE 24. Streamwise development of the Reynolds stress correlation coefficient as a function of the acceleration parameter K.

The behaviour of the Reynolds stress correlation is perhaps best summarized by figure 24 which presents the variation of $-\langle uv\rangle/\langle u^2\rangle^{1/2}\langle v^2\rangle^{1/2}$ as a function of the local acceleration parameter K for two representative wall-normal positions: $yu_\tau/\nu = 35$ and $yu_\tau/\nu = 400$. Note that as K increases, the Reynolds stress correlation coefficient initially increases at $yu_\tau/\nu = 400$, while it immediately decreases for the near-wall location. For both positions, however, large reductions are associated with the largest values of K. Note, however, that the minimum value of the correlation coefficient occurs downstream of maximum K. There is clearly a delay between the imposed external flow acceleration and the response of the Reynolds stress correlation, and this gives rise to hysteresis as shown in figure 24.

For an $Re_\theta = 862$ turbulent boundary layer characterized by a $K_{max} = 4.0 \times 10^{-6}$ pressure gradient, Warnack & Fernholz (1998 *b*) observed a reduction in the Reynolds shear stress correlation coefficient for $yu_\tau/\nu \leqslant 200$ and an increase for $yu_\tau/\nu \geqslant 200$ when compared to the ZPG turbulent boundary layer. Overall, this behaviour is consistent with the results of the current investigation in which progressive reduction in $-\langle uv\rangle/\langle u^2\rangle^{1/2}\langle v^2\rangle^{1/2}$ is observed in the near-wall region as the boundary layer is accelerated.

11.1. *Turbulence production*

The turbulence production in the boundary layer is a summation of the shear and dilatational components,

$$P_{tot} = -\langle uv\rangle \frac{\partial U}{\partial y} - (\langle u^2\rangle - \langle v^2\rangle)\frac{\mathrm{d}U_e}{\mathrm{d}x}. \tag{11.1}$$

In (11.1), the second term acts as a sink for turbulent kinetic energy, since $\langle u^2\rangle > \langle v^2\rangle$ throughout the boundary layer and $\mathrm{d}U_e/\mathrm{d}x > 0$. Hence, it is of interest to examine the variation of turbulence production with x/L.

Figure 25 presents the streamwise evolution of representative sample profiles of the total turbulence production as defined by (11.1) and scaled by ν/u_τ^4. These profiles are presented in terms of inner-variable, wall-normal coordinate scaling. At each streamwise location, peak turbulence production occurs near the wall; $yu_\tau/\nu \approx 15$ initially but shifts to approximately 20 wall units for the accelerated boundary layer. The effect of the external flow acceleration is to significantly reduce the scaled turbulence production with x/L. Although not presented here, measurements of the

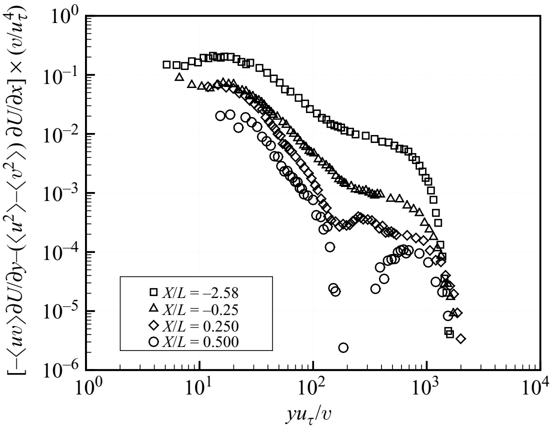

FIGURE 25. Streamwise development of the inner-variable-scaled total turbulence production, $-\langle uv\rangle(\mathrm{d}U(y)/\mathrm{d}y) - (\langle u^2\rangle - \langle v^2\rangle)(\mathrm{d}U_e/\mathrm{d}x)/(\nu/u_\tau^4)$.

unscaled shear production term $-\langle uv\rangle(\partial U/\partial y)$ exhibits peak values in the near-wall region that increase two orders of magnitude as the flow is accelerated. The absolute value of the dilatational term increases six orders of magnitude over the same streamwise distance. Despite this, in the near-wall region (say $yu_\tau/\nu < 100$) the shear production term always remains at least an order of magnitude larger than the absolute value of the dilatational term. Hence, even for the largest external flow acceleration encountered in the experiment, the near-wall turbulence production is always shear dominated, and the total turbulence production term remains positive. That the turbulence production does not scale with u_τ is a consequence of the local Reynolds stress not keeping pace with changes in the mean strain rate. The greatest reduction in scaled turbulence production occurs in the outer part of the boundary layer. Note that in the relaminarization region at $x/L = 0.25$, a cusp develops in the turbulence production profile. This cusp grows to becomes quite prominent by $x/L = 0.5$, where a zone of nearly zero turbulence production develops centred near $yu_\tau/\nu \approx 200$ ($y/\delta \approx 0.09$). At this location shear and dilatational production terms actually do become comparable in magnitude. In effect, for streamwise locations associated with the largest flow acceleration, the outer part of the boundary layer becomes essentially passive in terms of turbulence production. Rather, the dilatational production term serves to transfer-energy from the fluctuations back to the mean flow.

12. Conditional near-wall measurements

The previous sections document the effect of the imposed FPG on both the mean flow and turbulence statistics leading to relaminarization. It is well known that the Reynolds stress is largely the result of coherent near-wall dynamics like the burst-sweep sequence (e.g. Robinson 1991). Consequently, it is of interest to investigate how these coherent near-wall motions might be modified by the imposed external flow acceleration. It has already been noted that Kline *et al.* (1967) observed the cessation of turbulent bursting in the near-wall region of a relaminarized boundary layer. That work was based on visualization of the near-wall flow. In this section a series of extensive conditional hot-wire measurements are presented, which quantify the effect of the flow acceleration on the near-wall motions. To characterize the ejection and sweep processes, the quadrant splitting (QS) technique of Lu & Willmarth (1973) has been employed.

12.1. *QS measurements*

Lu & Willmarth (1973) found Reynolds stress production to be dominated by large-amplitude u- and v-motion of the near-wall turbulent boundary layer, which reside in the second ($u(t) < 0$, $v(t) > 0$) and fourth ($u(t) > 0$, $v(t) < 0$) quadrants. Second-quadrant ($Q2$) motions, often referred to as *ejections*, are thought to be associated with the lift-up of low-momentum fluid from the near-wall by counter-rotating streamwise vortices. These motions were found by Lu & Willmarth (1973) to account for 77 % of the Reynolds stress. Similarly, the $Q4$ motions, typically referred to as *sweeps*, are believed to be created by the down-draft of a convecting hairpin packet sweeping high-momentum fluid towards the wall. Lu & Willmarth (1973) found these $Q4$ events account for 55 % of the Reynolds stress (with the balance accounted for by $Q3$ and $Q1$ events). In simultaneous flow visualization and hot-film measurements, Bogard & Tiederman (1986) found the QS technique had the highest probability of identifying an ejection or sweep event as compared to other conditional measurement schemes like the VITA technique (Blackwelder & Kaplan 1976).

The QS method is implemented by determining the instants of time at which the $u(t), v(t)$ velocity components reside in a given quadrant and are above a specified threshold. As with the VITA technique, an identification (ID) function for each quadrant can be created and conditional statistics based on these functions may be calculated in a similar manner. The ID functions are created using the detection criteria:

$$ID_{Q2}(t) = \begin{cases} 1 & \text{if } u(t) < 0 \text{ and } u(t)v(t) < -\alpha_q \langle u^2\rangle^{1/2}\langle v^2\rangle^{1/2}, \\ 0 & \text{otherwise,} \end{cases} \tag{12.1}$$

$$ID_{Q4}(t) = \begin{cases} 1 & \text{if } u(t) > 0 \text{ and } u(t)v(t) < -\alpha_q \langle u^2\rangle^{1/2}\langle v^2\rangle^{1/2}, \\ 0 & \text{otherwise.} \end{cases} \tag{12.2}$$

Unless otherwise noted, a so-called hyperbolic hole of $\alpha_q = 1.5$ and a data record of 100 000 samples (corresponding to $18\,592 \leqslant tu_\tau^2/\nu \leqslant 800\,750$) were acquired at each x/L location for the reported results. A series of extensive preliminary tests was performed to ensure that the results of the conditional sampling measurements were not overly sensitive to the value of hole size α_q. The value $\alpha_q = 1.5$ used in these measurements was deemed optimum in this regard. In the boundary layer upstream of onset of flow acceleration, the application of the QS technique indicated that $Q2$ and $Q4$ events account for 78.8 % and 64 % of the Reynolds shear stress in the near-wall region, respectively, in good general agreement with Lu & Willmarth (1973).

Due to the imposed external flow acceleration and the consequent thinning of the boundary layer, the local characteristic eddy roll-over time scale associated with the largest scales in the flow, δ/U_e, decreases by nearly two orders of magnitude with streamwise distance. In examining the statistics of $Q2$ or $Q4$ events it can be deceptive to sample over a fixed time interval, since the flow acceleration serves to sweep more vortical flow structures past a fixed downstream measurement location per unit time. This effect of the flow acceleration on local $Q2/Q4$ statistics can be removed by examining $Q2$ or $Q4$ events during a fixed, but sufficiently large, number of local eddy roll-over times. For this investigation, a duration of 1000 local eddy roll-over times was chosen to compute QS statistics. This value was sufficient to provide fully converged statistics for all streamwise measurement locations.

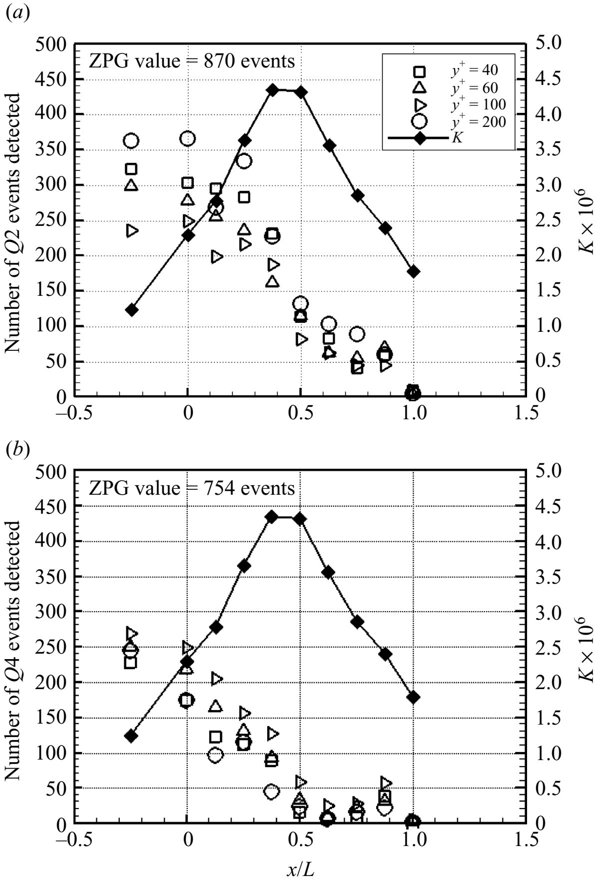

FIGURE 26. The streamwise evolution of the number of (*a*) $Q2$ and (*b*) $Q4$ events for 1000 eddy roll-over times measured at $yu_\tau/\nu = 40$, 60, 100 and 200. Shown for reference is the acceleration parameter K and the $x/L = -2.58$ ZPG value.

Figure 26 presents the streamwise variation in the number of $Q2$ and $Q4$ events detected during 1000 local eddy roll-over times. Also shown for reference is the streamwise variation in the acceleration parameter K. In each case, the streamwise variation in the number of $Q2$ and $Q4$ events detected is shown for several representative wall-normal positions ($40 \leqslant yu_\tau/\nu \leqslant 200$). Figure 26 shows that the effect of the FPG is to significantly reduce the number of $Q2$ and $Q4$ events detected. A steady reduction in the number of $Q2$ events is seen as the boundary layer is accelerated through the contraction. The most significant reduction in $Q2$ events occurs for $K > 3.3 \times 10^{-6}$ and corresponds with the onset of relaminarization. An even larger reduction in $Q4$ events occurs for $K > 2.5 \times 10^{-6}$ and ultimately results in fewer than 20 events detected for $x/L \geqslant 0.5$. The number of ejection and sweep events in the contraction is far smaller than the number measured upstream in the ZPG boundary layer (870 $Q2$ events and 754 $Q4$ events). Note also that the local number of $Q2$ and $Q4$ events shown in figure 26 is not strongly dependent on the wall-normal position within the range presented.

Figure 27 presents the streamwise variation in the corresponding mean time between successive $Q2$ and $Q4$ events, using inner-variable scaling, $T_{Q_i}u_\tau^2/\nu$. In this

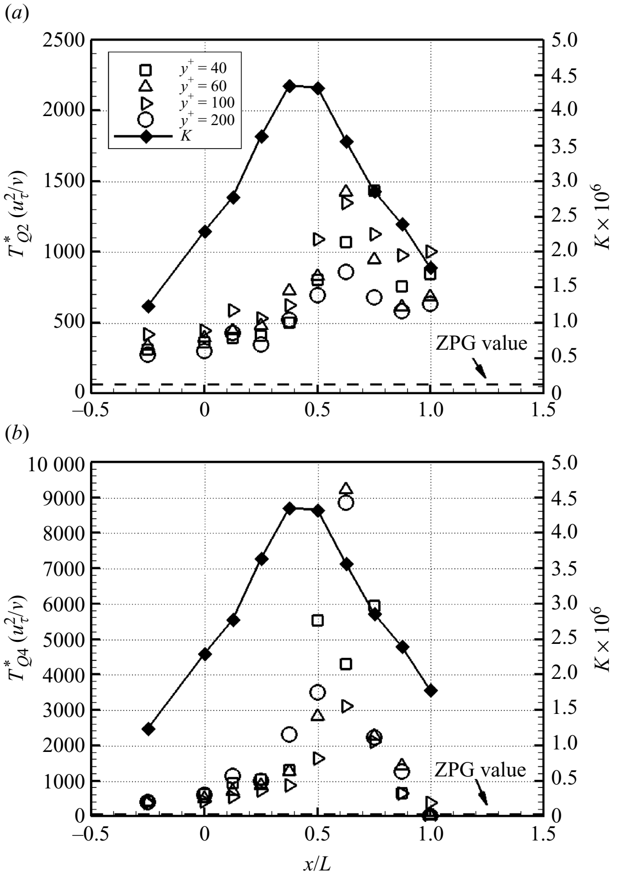

FIGURE 27. The streamwise evolution of the mean time between (*a*) $Q2$ and (*b*) $Q4$ events for 1000 eddy roll-over times measured at $yu_\tau/\nu = 40$, 60, 100 and 200. Shown for reference is the acceleration parameter K and the $x/L = -2.58$ ZPG value.

investigation, the mean time between events, T_{Q_i}, is based on the statistical mean of the measured probability density function for the time between detected events. Here again the statistics have been computed for a time interval equal to 1000 local eddy roll-over times. Also shown for reference is the streamwise variation in the acceleration parameter K. In each case, the streamwise variation in T_{Q_i} is shown for several representative wall-normal positions. However, the streamwise variation of T_{Q_i} is not a strong function of wall-normal coordinate. At all locations shown, the values of both T_{Q_2} and T_{Q_4} are much greater than their corresponding value for the ZPG boundary layer (which is indicated for reference). As K increases, so too does T_{Q_i}. At each x/L location it is found that $T_{Q_4} \gg T_{Q_2}$. Both T_{Q_2} and T_{Q_4} reach peak local values at $x/L = 0.625$, which is just downstream of the location at which K begins to decrease ($x/L = 0.5$). Hence, there appears to be a streamwise lag between the location of peak K and peak T_{Q_i}. The peak value of T_{Q_4} is particularly large, indicating the effective elimination of active $Q4$ events.

Consideration is next given to the number of $Q2$ and $Q4$ events above the threshold α_q normalized by the total number of $Q2$ or $Q4$ events (those both above and below the α_q threshold). This allows examination of the streamwise variation in the

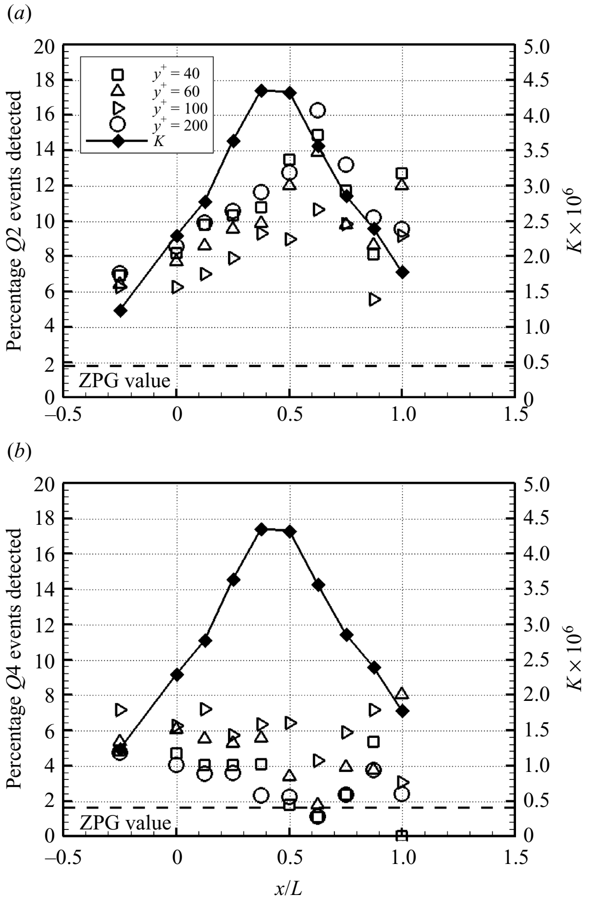

FIGURE 28. The streamwise evolution of percentage of (*a*) $Q2$ and (*b*) $Q4$ events for 1000 eddy roll-over times measured at $yu_\tau/\nu = 40$, 60, 100 and 200 that contribute to Reynolds stress production. Shown for reference is the acceleration parameter K and the $x/L = -2.58$ ZPG value.

percentage of local large-amplitude $Q2$ or $Q4$ events which contribute most to the Reynolds stress. These results, which are again based upon events detected during 1000 local eddy roll-over times, are shown in figure 28. Examination of figure 28 reveals that an increasing percentage of $Q2$ events are active (i.e. exceeding threshold, α_q) inside the contraction. In contrast, the percentage of active $Q4$ events decreases through the contraction.

Taken together, figures 26 and 28 suggest that while there are fewer $Q2$ events in the strong FPG boundary layer, the percentage of active $Q2$ events actually increases in relation to the number of background $Q2$ events. Ejections still occur but at a reduced rate compared to ZPG boundary layers. However, the remaining $Q2$ events tend to be of larger amplitude and more dynamically significant. This is consistent with the results shown previously in figure 19(*b*), indicating increasingly vigorous $\langle v^2 \rangle$ levels near the wall relative to u_τ. In contrast, figure 28 shows that the percentage of active $Q4$ events decreases in the region of the flow in which the acceleration parameter is largest. Hence there is a large decrease in both the total number and the

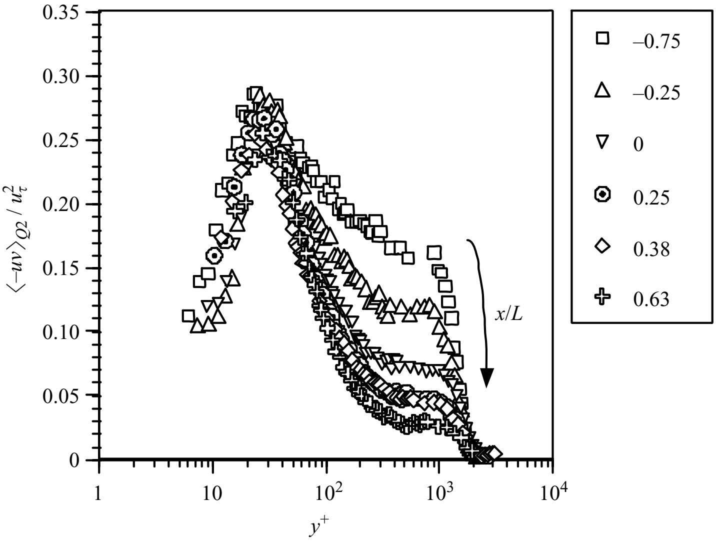

FIGURE 29. Inner-variable-scaled profiles of $-\langle uv \rangle|_{Q2}$, obtained at representative x/L locations.

relative percentage of active $Q4$ events. This indicates that sweep events are nearly entirely eliminated by the strong FPG.

Consideration is next given to the streamwise evolution of conditional Reynolds stress profiles associated with quadrants 1–4.

12.2. *Quadrant-dependent Reynolds stress*

Using the QS technique, profiles of $-\langle uv \rangle$ associated with each quadrant were obtained for a representative range of x/L, including the realminarized boundary layer. For these measurements the hyperbolic hole size $\alpha_q = 1.5$ as in the previously presented conditional measurements.

Figure 29 presents the streamwise evolution of $-\langle uv \rangle$ associated with $Q2$ (which is denoted $-\langle uv \rangle|_{Q2}$) normalized by u_τ^2. The wall-normal coordinate is presented using inner-variable scaling. This figure clearly shows a reduction in $-\langle uv \rangle|_{Q2}/u_\tau^2$ in the outer part of the boundary layer as the flow is accelerated. However, in the near-wall region, peak values of $-\langle uv \rangle|_{Q2}$ scale with u_τ. In particular, the profiles exhibit a peak value of $-\langle uv \rangle]_{Q2}/u_\tau^2 \approx 0.26$ at $yu_\tau/\nu \approx 20 - 25$. Representative x/L locations associated with relaminarization are included in figure 29, and the profiles of $-\langle uv \rangle|_{Q2}/u_\tau^2$ at these locations are shown to exhibit reasonable collapse for $yu_\tau/\nu \leqslant 250$.

Examination of unscaled profiles of $-\langle uv \rangle|_{Q2}$ (not presented) showed that for $y/\delta > 0.1$, the values of $-\langle uv \rangle|_{Q2}$ are essentially constant (i.e. frozen) with x/L giving rise to the reduction in $-\langle uv \rangle|_{Q2}/u_\tau^2$ shown in figure 29. In the near-wall region, however, $-\langle uv \rangle|_{Q2}$ increases significantly with x/L, with peak values occurring near $y/\delta = 0.006$. Figure 29 indicates this growth scales with inner variables, suggesting that the origin of the streamwise growth of $-\langle uv \rangle|_{Q2}$ is a consequence of near-wall streamwise vortices.

Figure 30 presents the streamwise evolution of profiles of $-\langle uv \rangle]_{Q4}/u_\tau^2$ in inner-variable scaling. This figure clearly shows that the effect of the external flow acceleration is to reduce $-\langle uv \rangle]_{Q4}/u_\tau^2$ over the entire boundary layer. Note also that the ordinate scale in figure 30 differs from that used in figure 29, so the near-wall $-\langle uv \rangle|_{Q4}$ levels are quite small compared to those associated with $Q2$. Unlike

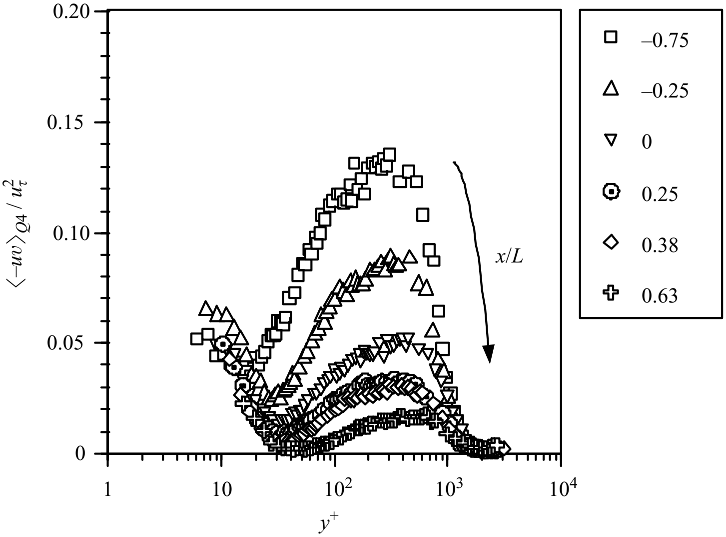

FIGURE 30. Inner-variable-scaled profiles of $-\langle uv\rangle|_{Q2}$, obtained at representative x/L locations.

the $Q2$ Reynolds stress, which exhibits strong near-wall streamwise growth, values of $-\langle uv\rangle|_{Q4}$ exhibit no significant increase. These results are consistent with the conditional measurements presented previously which showed that the effect of the external flow acceleration was to drastically reduce the number of $Q4$ 'sweep' events while less frequent but more energetic $Q2$ motions persist. It is important to note that this is in stark contrast to the behaviour observed in APG turbulent boundary layers by Krogstad & Skåre (1995) in which $Q2$ ejection events were eliminated while the number of sweep events and the $Q4$ contribution to Reynolds stress increased considerably in response to strong external flow deceleration.

Figure 31 presents the streamwise variation of profiles of $-\langle uv\rangle]_{Q3}/u_\tau^2$ in inner-variable scaling. Over most of the boundary layer ($yu_\tau/\nu > 100$) the $Q3$ contribution to Reynolds stress is essentially negligible. However, in the near-wall region, it is apparent that the streamwise flow acceleration gives rise to continuous growth of $-\langle uv\rangle|_{Q3}/u_\tau^2$ with the largest values occurring near $yu_\tau/\nu = 20$–25, which is the same wall-normal location associated with peak $-\langle uv\rangle|_{Q2}$. However, unlike the $Q2$ Reynolds stress, the $-\langle uv\rangle]_{Q3}$ profiles do not exhibit complete collapse with inner-variable scaling.

It is clear from figures 30 and 31 that the flow acceleration has the effect of both the near elimination of $Q4$ events and an increase in large amplitude $Q3$ events in the near-wall region. This, in turn, has the effect of significantly reducing the total near-wall Reynolds stress for streamwise locations associated with relaminarization. Indeed, this is the primary reason for the reduction in Reynolds stress correlation coefficient shown in figure 23 for wall-normal locations, $yu_\tau/\nu < 100$.

The acceleration-induced change in the character of the near-wall flow is also readily apparent upon simply examining the character of $u(t)$–$v(t)$ scatter plots obtained in the near-wall region at selected x/L locations. Figure 32 presents $u(t)$–$v(t)$ measurements obtained inside the contraction at $x/L = 0.75$ for several representative wall-normal locations. This figure clearly shows the development of large-amplitude fluctuations in $Q2$ and $Q3$, which are confined to the near-wall region; with increased distance

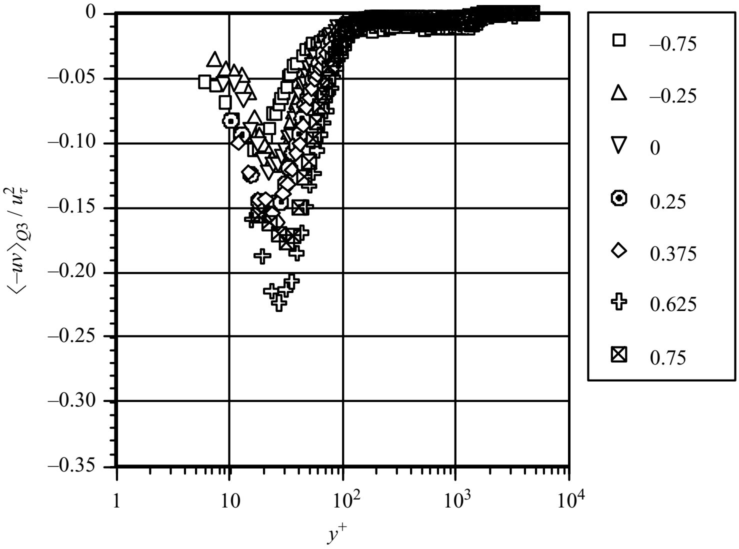

FIGURE 31. Inner-variable-scaled profiles of $-\langle uv \rangle|_{Q3}$, obtained at representative x/L locations.

from the wall, the scatter plots exhibit the more familiar preference for $Q2$ and $Q4$ that characterizes the upstream flow.

The QS method was applied to 400 000 sample $u(t)$, $v(t)$ time-series signals ($74\,370 \leqslant tu_\tau^2/\nu \leqslant 3\,203\,000$) obtained at several representative streamwise locations, each at various wall-normal locations. Results comparing the streamwise variation in the number of $Q3$ and $Q4$ events are shown in figure 33. This figure shows an apparent relationship between the streamwise decrease in the number of $Q4$ events (which was documented previously) and increase in the number of $Q3$ events. Note that the most significant changes are clearly associated with the region of largest flow acceleration. To examine this phenomenon further, the local number of $Q3$ and $Q4$ events are averaged over the multiple wall-normal positions shown (since there does not appear to be a large dependence on wall-normal location in figure 33). The number of $Q3$ and $Q4$ events associated with the initially ZPG boundary layer at $x/L = -2.58$ were then subtracted, giving the local change in the number of events from that occurring in the ZPG boundary layer (denoted $Q3^*$ and $Q4^*$). The resulting $Q3^*$ and $Q4^*$ data were curve-fitted and differentiated with respect to normalized streamwise distance x/L. Results are shown in figure 34. Also shown are $|\mathrm{d}Q3^*/\mathrm{d}(x/L)|$ (the streamwise rate of increase in $Q3$ events) and $|\mathrm{d}Q4^*/\mathrm{d}(x/L)|$ (the streamwise rate of decrease in $Q4$ events), the similarity between which is striking. This shows that the streamwise rate of increase in $Q3$ events matches the rate of decrease of $Q4$ events.

13. Discussion

13.1. *Comparison with adverse pressure gradient boundary layers*

Although the mean pressure gradient does not explicitly appear in the Reynolds stress transport equation, it directly influences the Reynolds stress gradient. Consequently, the turbulence production will also be influenced (as documented in this study). This implies, in turn, that the dynamic processes involving wall turbulence production are

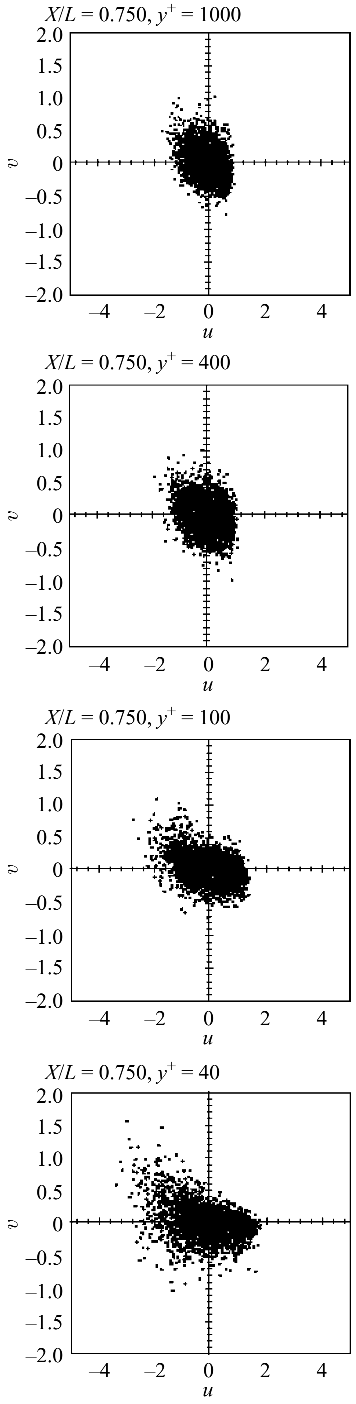

Figure 32. The $u(t)$ and $v(t)$ velocity components measured at $x/L = 0.75$ at representative wall-normal locations.

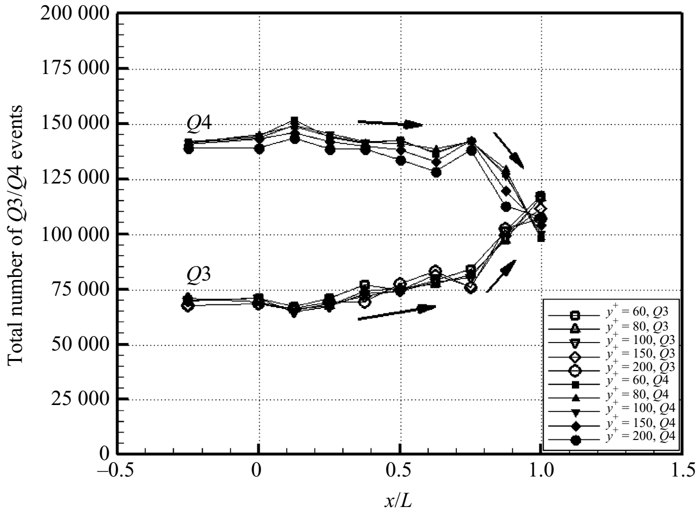

FIGURE 33. The streamwise evolution of the total number of $Q3$ and $Q4$ events at various wall-normal locations.

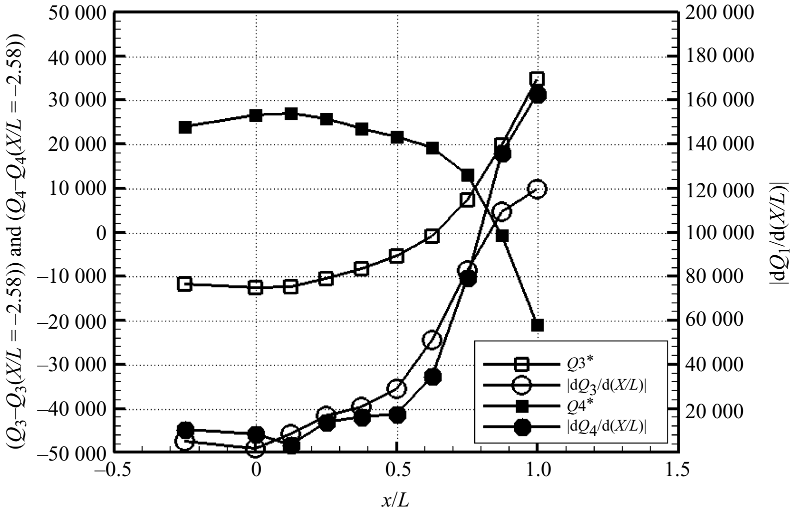

FIGURE 34. Averaged $Q3^*$ and $Q4^*$ profiles as functions of streamwise distance and the magnitude of their derivatives with respect to streamwise distance, $|\mathrm{d}Q3^*/\mathrm{d}(x/L)|$ and $|\mathrm{d}Q4^*/\mathrm{d}(x/L)|$.

influenced by the applied mean pressure gradient. This has been clearly demonstrated in a turbulent boundary layer that develops in strong *APG* by Krogstad & Skåre (1995). Conditional measurements utilizing the QS method showed the APG boundary layer to be totally dominated by $Q4$ (sweep) events with $Q2$ (ejection) events nearly absent. Thus, it was found that large-scale motions directed towards the wall were much more frequent and of longer duration in strong APG boundary layers. Their study also showed that the mean velocity outer wake defect was far larger than in the ZPG turbulent boundary layer. This behaviour is exactly opposite that observed in the FPG boundary layer that forms the focus of this study. As described earlier, the outer wake defect disappears, and conditional measurements show that $Q4$ events are virtually eliminated, while the number of $Q2$ events is significantly reduced. However, although reduced in number, the percentage of high-amplitude $Q2$ events actually increases in relation to the number of background $Q2$ events. Hence, the results of this study show that sweep motions are nearly eliminated, while near-wall ejection events that are of larger amplitude and more dynamically significant remain even in the relaminarized flow.

13.2. *On wall turbulence generation mechanisms*

The mechanism for the generation and sustenance of wall turbulence has typically been examined within the context of canonical ZPG turbulent boundary layers or fully developed channel flow. For boundary layer relaminarization to occur, the near-wall turbulence autogeneration cycle must be interrupted. Hence, it is useful to discuss the results of the present study in the context of previous work regarding the mechanisms of turbulence generation with particular focus on how the cycle might be modified by the streamwise straining.

It is now widely accepted that near-wall coherent structures play a key role in the generation and maintenance of boundary layer turbulence, though many of the details of the process are not fully understood. The topology of boundary layer coherent structures is discussed in the review by Robinson (1991), while wall turbulence generation mechanisms are described in the book edited by Panton (1997). A substantial body of work involving both experiments and large-scale numerical simulations show that coherent structures take the form of hairpin or horseshoe vortices in the turbulent boundary layer (e.g. Robinson 1991; Zhou *et al.* 1999; Marusic 2001). This structure consists of streamwise vortices that originate near the wall (i.e. the leg of the hairpin) but lift to form a spanwise arch that, in some cases, may extend to the outer region of the boundary layer. Robinson (1991) and Adrian (2007) describe how hairpin vortices are responsible, in large part, for the $Q2$ and $Q4$ events that lead to Reynolds stress production and wall-normal transport of momentum. Although hairpins are often idealized as symmetric, experiments involving high-resolution stereo particle image velocimetry by Stanislas, Perret & Foucaut (2008) show that the most probable structure is a one-legged hairpin vortex. Stanislas *et al.* (2008) also found that the boundary layer could be divided into two regions: for $y^+ < 150$ the boundary layer is densely populated with eddy structures that undergo mutual interaction. In the logarithmic region the interactions are much less frequent, and the primary evolution mechanism is vortex stretching by the mean flow and shear stresses.

Work by Adrian and colleagues (e.g. Adrian *et al.* 2000; Adrian 2007) suggests that hairpin vortices actually form in packets. This is consistent with the observations of Bogard & Tiederman (1986), which showed that a burst event actually consists of sequential $Q2$ ejection events. In the hairpin-packet model of Adrian (2007), the boundary layer at a given streamwise location consists of newly formed, slowly advecting hairpin packets in the near-wall region with older, more rapidly moving hairpin packets from the upstream flow located farther from the wall. Direct numerical simulation studies by Zhou *et al.* (1999) demonstrated the near-wall generation of nascent hairpin vortices, both upstream and downstream of the parent hairpin; a process termed autogeneration. This process appears quite robust with new hairpin vortices emerging in spite of artificially elevated levels of fine-scale background turbulence. In this manner, the autogeneration of hairpin vortices and the formation of hairpin packets becomes a key aspect of the wall turbulence generation process.

The significant wall-normal extent of the hairpin structures also suggests the possibility of a coupling of the dynamic processes of the near-wall and outer regions of the boundary layer. Several studies support this idea; for example, Kobashi & Ichijo (1986) found that low-frequency pressure fluctuations measured in the near-wall region are correlated with large-scale motions in the outer portion of the boundary layer. It was suggested that the turbulent burst sequence is phase related to the outer large-scale motions. A low-order dynamical-system model of the near-wall region of a turbulent boundary layer was developed by Aubry & Stone (1988) who utilized the proper orthogonal decomposition eigenfunctions obtained in turbulent pipe flow experiments by Herzog (1986). The model duplicated the experimentally observed dynamical behaviour of streamwise roll formation and also included the occurrence of intermittent ejection and burst-like events. It was found that pressure signals from the outer part of the boundary layer triggered the burst process and determined its frequency. Myose & Blackwelder (1994) also highlighted the importance of spanwise vorticity in the outer part of the boundary layer on the near-wall turbulence production process. In particular, their results show that wall-eddy breakdown could be triggered by the streamwise acceleration associated with the outer region of the turbulent boundary layer.

In contrast to the studies cited above, numerical experiments on turbulent channel flow by Jimenez & Pinelli (1999) showed quite convincingly that a near-wall turbulence production cycle exists, which is essentially independent of the outer flow. This was demonstrated by artificially manipulating the outer flow in numerical simulations and observing what effect, if any, this had on the near-wall turbulence production. The study showed that low-speed streak formation in the near-wall region was caused by the advection of the mean profile by streamwise vortices. The streamwise vortices, in turn, originated from an instability (presumed inflectional by the authors) of the low-speed streak. Manipulations of the outer flow were found to have little influence on this process, thereby indicating its autonomous character. Similarly, it was shown that the turbulence generation mechanism was not directly linked to the presence of the wall; the wall serves only to provide the necessary mean shear. The authors cautioned that mechanisms based upon interactions between inner and outer regions of wall-bounded turbulent flows (like those described in previously cited studies) may well exist. They concluded, however, that in high-Reynolds-number flows in which multiple mechanisms coexist, the near-wall streak/streamwise vortex autogeneration mechanism will dominate. More recently, Schoppa & Hussain (2002) demonstrated that near-wall streamwise coherent structures originate from a sinuous instability of lifted, vortex-free low-speed streaks. It was shown that lifted streaks can undergo a sinuous normal mode of instability which exhibits twofold amplification. More significantly, the authors described a streak transient growth instability of x-dependent spanwise velocity disturbances leading to an order-of-magnitude amplification culminating in the formation of streamwise vortices via nonlinear processes. The instantaneous characteristics of the resulting near-wall vortices are consistent with those educed from conditional measurements in fully turbulent flows. Critical to the instability leading to the formation of longitudinal near-wall vortices is the wall-normal vorticity flanking lifted low-speed streaks. Schoppa & Hussain (1998) exploited this dependence to demonstrate turbulent boundary layer drag reduction. This is accomplished through simulations of actuation which serves to weaken the streak flank wall-normal vorticity and thereby suppress the underlying instability mechanism.

13.3. *On the dual-layer structure of the accelerated boundary layer*

Many of the measurements presented in this study show that the boundary layer develops a dual-layer structure that is in some respects reminiscent of the two-layer model for relaminarization proposed by Sreenivasan (1982). That model is comprised of a viscous inner layer in which turbulence is in decay and an effectively inviscid outer layer in which the Reynolds stresses are frozen. Sreenivasan (1982) attributed relaminarization to 'the domination of pressure forces over the slowly responding Reynolds stresses in the outer-layer, accompanied by the generation of a new laminar sub-boundary layer, which itself is maintained stable by the acceleration.' In this study the onset of relaminarization (as evidenced by initial reduction in c_f) is characterized by $(\mathrm{d}P/\mathrm{d}x)/(\tau_w/\delta) \approx 400$. However, the largest reduction in c_f is associated with $(\mathrm{d}P/\mathrm{d}x)/(\tau_w/\delta) > 2000$. It is found that the outer layer comprises most of the wall-normal extent of the boundary layer (say $y/\delta > 0.1$). In this region the turbulent normal and shear stresses do not scale with u_τ or U_e and are instead effectively 'frozen' (or in slow decay). In contrast, the near-wall region appears dynamically active with turbulent stresses actually exhibiting streamwise growth with the imposed flow acceleration (e.g. figure 17). Despite this observed streamwise growth, inner-variable-scaled near-wall turbulence production is reduced by an order of magnitude by the imposed FPG. In comparison, scaled turbulence production in the outer boundary layer is reduced by over three orders of magnitude due to the fact that the shear and dilatational turbulence production terms become comparable there (see figure 25).

The dual-layer nature of the relaminarizing boundary layer is perhaps most apparent from examination of profiles of the Reynolds stress correlation as shown in figures 23 and 24. These show that the Reynolds stress correlation is most strongly effected in the near-wall region in which it decreases to take on very small values at x/L locations associated with relaminarization. In comparison, larger values are maintained in the outer portion of the boundary layer, and this is likely associated with the streamwise straining of vortical structures that originate in the upstream flow. The presence of hysteresis in the relaminarization region indicates the delayed response of the Reynolds stress to the imposed external flow acceleration.

13.4. *Effect of acceleration on stabilizing the near-wall region*

A key element in the wall turbulence generation mechanism described by Schoppa & Hussain (2002) is lifted low-speed streaks that extend even beyond the buffer layer. These are quite distinct from the more numerous sublayer streaks which are confined to the viscous sublayer. Schoppa & Hussain (2002) characterized the strength of the lifted streaks in terms of the maximum inclination angle of vortex lines on the streak flank, θ_v. Their stability calculations demonstrated a threshold value of θ_v below which the streaks are found to be stable. In this manner, the strength of the lifted streak at some wall-normal location, y^+, is dependent on the ratio of the streak flank wall-normal vorticity component ω_y to the local spanwise vorticity $\omega_z \approx \mathrm{d}U/\mathrm{d}y)_{y^+}$.

A consequence of the streamwise straining of near-wall vortices by the imposed FPG is an increase in spanwise separation of near-wall streamwise vortices due to mutual induction. This has a related effect on low-speed streak formation and spanwise spacing. Finnicum & Hanratty (1988) found that near-wall streak spacing was fairly insensitive to APGs. In contrast, the spacing was quite sensitive to favourable gradients with large increases occurring for the strong gradients associated with relaminarization. This behaviour was observed in the present study by Bourassa (2005), where a large increase in mean streak spacing above the nominal ZPG value of

$\lambda_z^+ = 100$ was reported. This was also the case in the study by Talamelli, Fomacian & Westin (2002). The observed increase in spanwise streak spacing would be expected to reduce the local value of ω_y. This, in combination with the acceleration-induced increase in $\omega_z \approx \mathrm{d}U/\mathrm{d}y)_{y^+}$, will have the effect of reducing the strength of elevated streaks (as characterized by θ_v). In this manner the number of elevated streaks would be reduced in the region of strong FPG, thereby reducing the formation of new streamwise vortices. Indeed, Schoppa & Hussain (2000*b*) noted the straightening of streak vorticity by ω_z is a strongly stabilizing effect for sinuous streak instability. The stabilization of low-speed streaks is consistent with the reduction in the number of $Q2$ ejection events observed in this study during a fixed number of local eddy roll-over time scales. Similar behaviour has also been noted in the large-scale numerical simulations of Piomelli, Balaras & Pascarelli (2000).

Measurements of the streamwise macroscale Λ_x made by Bourassa (2005) show that the effect of the FPG is to dramatically increase the characteristic length of flow structures with streamwise distance. Warnack & Fernholz (1998*b*) measured a similar increase of the longitudinal integral length scale and in addition observed a decrease in wall-normal macroscale Λ_y in an accelerated turbulent boundary layer with $K \leqslant 4.0 \times 10^{-6}$. As a consequence, near-wall streamwise vortices will experience considerable dilatation at x/L locations associated with maximum K. As they are stretched, conservation of angular momentum requires that their rotational motions undergo a commensurate increase. In this manner, transfer of low-momentum fluid away from the wall comes about due to energetic wall-normal motion induced by the stretching of streamwise-oriented vortices inside the viscous wall region. Although the number of streamwise vortices is reduced due to the stabilizing effect of mean shear, for those that do form, streamwise stretching is expected to give rise to particularly vigorous wall-normal motion which is consistent with the observation of less frequent but more robust $Q2$ ejection events in the relaminarizing flow. Since the origin of the measured $Q2$ events are strained streamwise vortices confined to the near-wall region, it is not surprising that the resulting $Q2$ Reynolds stress shown in figure 29 scales on inner variables for $y^+ < y_o^+$ (see figure 15) and peaks in the relaminarizing flow.

13.5. *The effective aliasing of $Q4$ events*

Conservation of mass requires that the transport of low-momentum fluid away from the wall by streamwise vortices be balanced by fluid transport back towards the near-wall region. In mild, favourable ZPG and APG boundary layers, wall-directed fluid motion from the outer boundary layer would transport comparatively high-momentum fluid towards the wall, which would be manifest as $Q4$ events. In this manner, for comparatively mild flow acceleration, stretching of streamwise vortices gives rise to more vigorous $Q2/Q4$ motions with an associated increase in wall-normal momentum transport and a consequent increase in the skin friction coefficient as shown in figure 5. In fact, for streamwise locations upstream of relaminarization, profiles of k/U_e^2 exhibit collapse near the wall with a peak value of $k/U_e^2 \approx 0.006$ occurring near $y/\delta = 0.01$. Blackwelder & Kovasznay (1972) also observed that the boundary layer kinetic energy scales with U_e^2 very near the wall. Note, however, that the near-wall scaling of k with U_e^2 breaks down for the streamwise locations associated with realminarization.

In the relaminarizing boundary layer, $Q2$ events are reduced in number, while $Q4$ events are nearly absent, and measurements indicate an altered interaction between the outer and near-wall regions of the boundary layer. Due to the very large value of $\mathrm{d}U_e/\mathrm{d}x$ at streamwise locations near relaminarization, a wall-directed fluid parcel

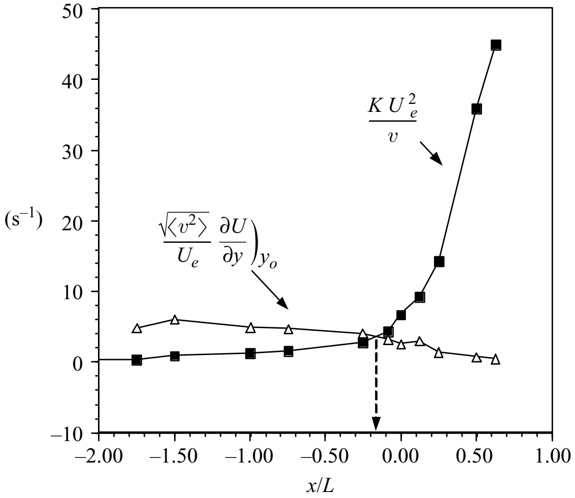

FIGURE 35. Variation of streamwise and cross-stream velocity gradient parameters with x/L.

can find itself in a region in which its streamwise momentum is actually lower than the local near-wall fluid, thereby giving rise to a ‘negative streamwise fluctuation associated with wall-directed motion’ – a $Q3$ event. In this manner, there can be an effective ‘aliasing’ of $Q4$ events into the third quadrant as a consequence of the large streamwise flow acceleration. This conjecture is supported by the experimental observation that associated with the streamwise reduction in the number of $Q4$ events, there is a matching increase in the number of $Q3$ events and that this effect increases with K (see figures 33 and 34). As shown in figure 31, $|-\langle uv\rangle|_{Q3}|$ increases in the near-wall region for the largest values of K, which has the effect of significantly reducing the total near-wall Reynolds stress for streamwise locations associated with relaminarization. As expected, peak values of $-\langle uv\rangle|_{Q3}$ occur at the same y^+ location as does peak $-\langle uv\rangle|_{Q2}$. The values of $-\langle uv\rangle|_{Q3}$ are found to be insignificant for $y/\delta > 0.1$.

A kinematic constraint for $Q4$ events to be effectively aliased to $Q3$ is easily derived based on the relative sizes of local streamwise and wall-normal mean velocity gradients. In particular, it may be shown that aliasing of $Q4$ events into $Q3$ requires that $KU_e^2/\nu > (\sqrt{\langle v^2\rangle}/U_e)\ \mathrm{d}U/\mathrm{d}y)_{y_o}$. Figure 35 plots both terms as functions of x/L. The figure shows that the above inequality is satisfied in the experiment for $x/L > -0.15$. Thus the constraint is satisfied at all streamwise locations associated with relaminarization. Note also that figure 33 shows the greatest reduction in $Q4$ events, and associated increase in $Q3$ events occurs just downstream of this location.

The apparent loss of high-momentum sweep events associated with the extreme flow acceleration encountered in the experiments gives rise to an effective decoupling of the inner and outer regions of the boundary layer in terms of wall-normal transport of streamwise momentum. The near-wall dynamics of the highly accelerated turbulent boundary layer are dominated by $Q3$ and $Q2$ motions that serve to transfer fluid to and away from the wall, respectively, due to streamwise vortices that reside in a dramatically thickened viscous layer. This, in turn, significantly reduces the near-wall Reynolds stress correlation.

Since there is reduced interaction between near wall and outer flow, profiles of $\langle u^2\rangle$ in the relaminarizing boundary layer exhibit collapse when scaled using inner variables (e.g. figure 18*b*). The peak value of $\langle u^2\rangle/u_\tau^2 \approx 3.6$ occurs near $yu_\tau/\nu \approx 23$ (a much lower peak value and located farther from the wall than in the ZPG boundary layer). Turbulence production mechanisms direct energy into streamwise fluctuations first, which are subsequently redistributed to other fluctuating components. Hence, it is not surprising that inner-variable-scaled profiles of $\langle v^2\rangle$ and $\langle w^2\rangle$ also exhibit collapse, downstream of where this first occurs for $\langle u^2\rangle$. The inner-variable scaling of profiles of normal stress is also consistent with the very rapid growth in thickness of the viscous wall layer in the relaminarization region.

Due to the stabilization of the near-wall flow by the increased spanwise vorticity and the elimination of sweep events, wall-normal motions reside predominantly in $Q2$ and $Q3$ which has the effect of reducing the Reynolds stress correlation and the wall-normal transport of momentum. As a consequence the skin friction coefficient drops rather dramatically as shown in figure 5, which is one of the hallmarks of boundary layer relaminarization. As discussed below, the streamwise variation in the Kármán constant shown in figure 11 is also consistent with a reduction in effective cross-stream transport of momentum with respect to the active flow as the boundary layer is exposed to the streamwise acceleration.

13.6. *Mean flow edistortion in the accelerated boundary layer*

The boundary layer mean velocity profiles exhibit considerable distortion in response to the strong external flow acceleration. As described earlier, this involves a complete loss of the outer wake defect profile and a substantial increase in thickness of the combined viscous sublayer and buffer regions. As shown in figure 15, the growth in thickness of the viscous near-wall region is approximately exponential near commencement of relaminarization. A logarithmic region is maintained even for the largest flow accelerations encountered in the experiment, although the slope $1/\kappa$ and additive constant B exhibit a systematic streamwise variation from standard ZPG values. For the logarithmic region, the variation of the Kármán and additive constants with applied pressure gradient is not explicitly associated with the relaminarization process. Systematic variation of the constants from their standard ZPG value occurs even for the comparably small FPG upstream of the contraction. In fact, figure 13 shows that the sensitivity of κ to imposed strain rate $\mathrm{d}U_e/\mathrm{d}x$ is actually greatest near ZPG. It is parenthetically noted that this sensitivity may explain disparate values of κ reported in the literature for ZPG boundary layers if those experiments are actually performed under pressure gradient conditions that are even slightly favourable. Upstream of the contraction, the measured variation in κ is fully consistent with the empirical correlation proposed by Nagib & Chauhan (2008) for a wide variety of turbulent boundary layer experiments in FPG and APG. However, the measurements obtained in this study extend the data set to much larger values of κB and B associated with strong FPGs and relaminarization. Perhaps more significant is the observation that the variation of κ and B occurs smoothly, without sudden change, as the boundary layer undergoes relaminarization (see figure 12).

It is well known that the log law can be derived from the premise that turbulence production locally balances dissipation. The profile is then determined by inertial transfer between eddies of length scale $\ell = \kappa y$, the characteristic eddy length scale being proportional to distance from the wall. This is consistent with the hairpin-packet model of Adrian and co-workers. As noted by Adrian (2007), one implication of that model is that at a fixed streamwise location, the boundary layer contains sequentially older and larger hairpin packets (that originate farther upstream) as one traverses the local boundary layer from the wall to outer region. With this in mind, the streamwise increase in the values of κ measured in this study is also consistent with this layered vortex-packet concept. At fixed wall-normal distance y, the streamwise increase in κ is indicative of an increased local characteristic eddy length scale as older hairpin packets from farther upstream, which have undergone a larger cumulative streamwise dilatation (in response to the accelerated free-stream flow), are encountered. This stretching of vortical structures in the outer part of the flow is consistent with the recent results of Stanislas *et al.* (2008). The experimental observation from this study that the logarithmic region commences farther from the wall with increased K is consistent with the stabilization of the near-wall region which gives rise to a consequent reduction in the formation of nascent hairpin vortices.

The authors would like to recognize the financial support of NASA Dryden Flight Research Center under grant NAG4-123 monitored by David Fisher.

REFERENCES

Adrian, R. 2007 Hairpin vortex organization in wall turbulence. *Phys. Fluids* **19** (4), 041301.

Adrian, R., Meinhart, C. & Tomkins, C. 2000 Vortex organization in the outer region of the turbulent boundary layer. *J. Fluid Mech.* **422**, 1–54.

Aubry, N., H. P. L. J. & Stone, E. 1988 The dynamics of coherent structures in the wall region of the turbulent shear layer. *J. Fluid Mech.* **192**, 1–33.

Badri Narayanan, M., Rajagopalan, S. & Narasimha, R. 1977 Experiments on the fine structure of turbulence. *J. Fluid Mech.* **80**, 237.

Badri Narayanan, M. & Ramjee, V. 1969 On the criteria for reverse transition in a 2-d boundary layer flow. *J. Fluid Mech.* **35**, 225–241.

Baranblatt, G. I. 1993 Scaling laws for fully developed turbulent shear flows. Part 1. Basic hypotheses and analysis. *J. Fluid Mech.* **248**, 513–520.

Baranblatt, G. I., Chorin, A. J. & Prostokishin, V. M. 2000 Self-similar intermediate structures in turbulent boundary layers at large Reynolds numbers. *J. Fluid Mech.* **410**, 263–283.

Blackwelder, R. & Haritonidis, J. 1983 Scaling of the bursting frequency in turbulent boundary layers. *J. Fluid Mech.* **132**, 87–103.

Blackwelder, R. & Kaplan, R. 1976 On the wall structure of the turbulent boundary layer. *J. Fluid Mech.* **76**, 89–112.

Blackwelder, R. & Kovasznay, L. 1972 Large-scale motion of a turbulent boundary layer during relaminarization. *J. Fluid Mech.* **53**, 61–83.

Bogard, D. & Tiederman, W. 1986 Burst detection with single-point velocity measurements. *J. Fluid Mech.* **162**, 389–413.

Bourassa, C. 2005 An experimental investigation of an accelerated turbulent boundary layer. PhD dissertation, University of Notre Dame, Notre Dame, IN.

Chauhan, K. A. 2007 Study of canonical wall-bounded turbulent flows. PhD dissertation, Illinois Institute of Technology, Chicago, IL.

Coles, D. 1956 The law of the wake in the turbulent boundary layer. *J. Fluid Mech.* **1**, 191–226.

van Dam, C., Vijgen, P., Yip, L. & Potter, R. 1993 Leading-edge transition and relaminarization phenomena on a subsonic high-lift system. *Paper* 93-3140. AIAA.

DeGraff, D. S. & Eaton, J. K. 2000 Reynolds-number effects of the flat-plate turbulent boundary layer. *J. Fluid Mech.* **422**, 319–346.

Dixit, S. A. & Ramesh, O. N. 2008 Pressure-gradient dependent logarithmic laws in sink flow turbulent boundary layers. *J. Fluid Mech.* **615**, 445–475.

Driver, D. M. 1998 Application of oil film interferometry skin-friction to large wind tunnels. In *Advanced Aerodynamic Measurement Technology, AGARD Conference Proceedings CP-601*, pp. 25-1–25-10. AGARD.

Dunn, P. F. 2005 *Measurement and Data Analysis for Engineering and Science*. McGraw-Hill.

Escudier, M., Abdel-Hameed, A., Johnson, M. & Sutcliffe, C. 1998 Laminarisation and re-transition of a turbulent boundary layer subjected to favourable pressure gradient. *Exp. Fluids* **25**, 491–502.

Escudier, M., Ramadan, A. & Johnson, M. 2001 Response of a skewed turbulent boundary layer to favourable pressure gradient. *Exp. Fluids* **30**, 657–671.

Fernholz, H. H. & Finley, P. J. 1996 The incompressible zero-pressure gradient turbulent boundary layer: an assessment of the data. *Prog. Aerosp. Sci.* **32**, 245–311.

Finnicum, D. S. & Hanratty, T. J. 1988 Effect of favourable pressure gradients on turbulent boundary layers. *AIChe J.* **34**, 529–540.

George, W. K. 2006 Recent advancements toward understanding turbulent boundary layers. *AIAA J.* **44**,11, 2435–2449.

George, W. K. & Castillo, L. 1997 Zero-pressure gradient turbulent boundary layer. *Appl. Mech. Rev.* **47**, 307–365.

Herzog, S. 1986 The large scale structure in the near wall region of turbulent pipe flow. PhD thesis, Cornell University, Ithaca, NY.

Ichimiya, M., Nakamura, I. & Yamashita, S. 1998 Properties of a relaminarizing turbulent boundary layer under a favourable pressure gradient. *Exp. Therm. Fluid Sci.* **17**, 37–48.

Jimenez, J. & Pinelli, A. 1999 The autonomous cycle of near-wall turbulence. *J. Fluid Mech.* **389**, 335–359.

Jones, M. B., Marusic, I. & Perry, A. E. 2001 Evolution and structure of sink flow turbulent boundary layers. *J. Fluid Mech.* **428**, 1–27.

Jones, W. & Launder, B. 1972 The prediction of laminarization with a two-equation model of turbulence. *Intl J. Heat Mass Transfer*. **15** (2), 301–314.

Julien, H., Kays, W. & Moffat, R. J. 1969 The turbulent boundary layer on a porous plate: experimental study of the effects of a favourable pressure gradient. *Tech Rep.* HMT-4. Stanford University Thermoscience Division.

Kapil, A. C., Nagib, H. M. & Monkewitz, P. 2005 Evidence of non-universality of Kármán constant. In *Proceedings of iTi Conference on Turbulence*, Bad Zwischenahn, Germany.

Klebanoff, P. 1955 Characteristics of turbulence in a boundary layer with zero pressure gradient. *Tech Rep.* 3178. NACA.

Kline, S., Reynolds, W., Schraub, F. & Runstadler, P. 1967 The structure of turbulent boundary layers. *J. Fluid Mech.* **30**, 741–773.

Kobashi, Y. & Ichijo, M. 1986 Wall pressure and its relation to turbulent structures of the turbulent boundary layer. *Exp. Fluids* **4**, 49.

Krogstad, P. & Skåre, P. 1995 Influence of strong adverse pressure gradient on the turbulent structure in a boundary layer. *Phys. Fluids* **7**, 2014–2024.

Launder, B. 1963 The turbulent boundary layer in a strongly negative pressure gradient. *Tech Rep.* 71. MIT Gas Turbine Lab.

Launder, B. 1964 Laminarization of the turbulent boundary layer by acceleration. *Tech Rep.* 77. MIT Gas Turbine Lab.

Liu, X. & Thomas, F. 2004 An experimental investigation of symmetric and asymmetric turbulent wake development in pressure gradient. *Phys. Fluids* **16** (5), 1725–1745.

Loyd, R. J., Moffat, R. J. & Kays, W. M. 1970 The turbulent boundary layer on a porous plate: an experimental study of the fluid dynamics with strong favourable pressure gradient and blowing. *Tech Rep.* MMT-13. Stanford University Thermoscience Division.

Lu, S. & Willmarth, W. 1973 Measurements of the structure of the Reynolds stress in a turbulent boundary layer. *J. Fluid Mech.* **60**, 481–511.

Marusic, I. 2001 On the role of large-scale structures in wall turbulence. *Phys. Fluids* **13** (3), 735–743.

Mathieu, S. & Scott, J. 2000 *An Introduction to Turbulent Flow*. Cambridge University Press.

Monkewitz, P. A., Chauhan, K. A. & Nagib, H. M. 2008 Comparison of mean flow similarity laws in zero pressure gradient turbulent boundary layers. *Phys. Fluids*. **20**, 105102.

Monson, D., Mateer, G. & Menter, F. 1993 Boundary-layer transition and global skin friction measurements with an oil-fringe imaging technique. *Paper* 932550. SAE.

Moretti, P. & Kays, W. 1965 Heat transfer in turbulent boundary layer with varying free stream velocity and varying surface temperature – an experimental study. *Intl J. Heat Mass Transfer* **8**, 1187.

Morrison, J., Subramanian, C. & Bradshaw, P. 1992 Bursts and the law of the wall in turbulent boundary layers. *J. Fluid Mech.* **241**, 75–108.

Mukund, K., Viswanth, P. R., Narasimha, R. & Crouch, J. 2006 Relaminarization in highly favourable pressure gradients on a convex surface. *J. Fluid Mech.* **566**, 97–115.

Myose, R. & Blackwelder, R. 1994 On the role of the outer region in the turbulent boundary layer bursting process. *J. Fluid Mech.* **259**, 345.

Nagib, H. M. & Chauhan, K. A. 2008 Variations of von Kármán coefficient in canonical flows. *Phys. Fluids* **20**, 101518.

Nagib, H., Christophorou, C. & Monkewitz, P. 2004 High Reynolds number turbulent boundary layers subjected to various pressure-gradient conditions. In *IUTAM 2004: One Hundred Years of Boundary Layer Research*. DLR Gottingen Germany, August 12–14 2004.

Narasimha, R. & Sreenivasan, K. 1973 Relaminarization in highly accelerated turbulent boundary layers. *J. Fluid Mech.* **61**, 417–447.

Narasimha, R. & Sreenivasan, K. 1979 Relaminarization of fluid flows. *Adv. Appl. Mech.* **19**, 221–309.

Oberlack, M. 2001 Unified approach for symmetries in plane parallel turbulent shear flows. *J. Fluid Mech.* **427**, 299–328.

Österlund, J. M. 1989 Experimental studies of zero pressure-gradient turbulent boundary-layer flow. PhD thesis, Department of Mechanics, Royal Institute of Technology, Stockholm.

Panton, R. L. (Ed.) 1997 *Self Sustaining Mechanisms of Near-Wall Turbulence*. Advances in Fluid Mechanics, vol. 15. Computational Mechanics.

Patel, V. 1965 Calibration of the Preston tube and limitations on its use in pressure gradients. *J. Fluid Mech.* **23**, 185.

Patel, V. & Head, M. 1968 Reversion of turbulent to laminar flow. *J. Fluid Mech.* **34**, 371–392.

Piomelli, U., Balaras, E. & Pascarelli, A. 2000 Turbulent structures in accelerating boundary layers. *J. Turbul.* **1**, 1.

Robinson, S. 1991 Coherent motions in the turbulent boundary layer. *Annu. Rev. Fluid Mech.* **23**, 601–639.

Schoppa, W. & Hussain, F. 1998 A large-scale control strategy for drag reduction in turbulent boundary layers. *Phys. Fluids* **10**, 1049–1051.

Schoppa, W. & Hussain, F. 2000*a* Coherent structure dynamics in near-wall turbulence. *Fluid Dyn. Res.* **26**, 119–139.

Schoppa, W. & Hussain, F. 2000*b* Generation of near-wall coherent structures in a turbulent boundary layer. *Current Sci.* **79** (6), 849–858.

Schoppa, W. & Hussain, F. 2002 Coherent structure generation in near-wall turbulence. *J. Fluid Mech.* **453**, 57–108.

Sreenivasan, K. R. 1982 Laminarescent, relaminarizing, and retransitional Flows. *Acta Mech.* **44**, 1–48.

Stanislas, M., Perret, L. & Foucaut, J.-M. 2008 Vortical structures in the turbulent boundary layer: a possible route to a universal representation. *J. Fluid Mech.* **602**, 327–382.

Talamelli, A., Fomacian, N. & Westin, K. 2002 Experimental investigation of streaky structures in a relaminarizing boundary layer. *J. Turbul.* **3**, 18.

Taylor, G. 1938 The spectrum of turbulence. *Proc. R. Soc. Lond.* A **164**, 476–490.

Warnack, D. & Fernholz, H. 1998*a* The effects of a favourable pressure gradient and of the Reynolds number on an incompressible axisymmetric turbulent boundary layer. Part 1. The boundary layer. *J. Fluid Mech.* **359**, 329–356.

Warnack, D. & Fernholz, H. 1998*b* The effects of a favourable pressure gradient and of the Reynolds number on an incompressible axisymmetric turbulent boundary layer. Part 2. The boundary layer with relaminarization. *J. Fluid Mech.* **359**, 357–381.

Wilson, D. G. and Pope, J. A. 1954 Convective heat transfer to gas turbine blades. *Proc. Inst. Mech. Eng.* **168**, 861.

Zhou, J., Adrian, R., Balachandar, S. & Kendall, T. 1999 Mechanisms for generating coherent packers of hairpin vortices in channel flow. *J. Fluid Mech.* **387**, 3563–396.

Zilliac, G. 1996 Further developments of the fringe-imaging skin friction technique. *Tech Rep.* 110425. NASA.

Zilliac, G. 1999 The fringe-imaging skin friction technique PC application user's manual. *Tech Rep.* 208794. NASA.